Regulation of TGF-β signaling and EMT in cancer progression

Zhang, J.

Chapter 6

A-series gangliosides inhibit TGF-β-induced epithelial-to-mesenchymal transition via TβRI degradation

Jing Zhang[1], Jin Ma[1,4], Hailiang Mei[2], Cedrick C. Agaser[2], Birol Cabukusta[1], Katarina Madunic[3], Gerard van der Zon[1], Manfred Wuhrer[3], Tao Zhang[3]* and Peter ten Dijke[1]*

[1]Oncode Institute and Cell Chemical Biology, Leiden University Medical Center, 2300 RC Leiden, The Netherlands.

[2]Sequence Analysis Support Core, Leiden University Medical Center, 2300RC Leiden, The Netherlands.

[3]Center for Proteomics and Metabolomics, Leiden University Medical Center, Leiden, The Netherlands.

[4]Present address: Shenzhen Jingtai Technology Co., Ltd, Floor 3, Sf Industrial Plant, Futian District, Shenzhen, China.

Manuscript in revision

Abstract

Epithelial-mesenchymal transition (EMT) is of pivotal importance in the development and initiation of cancer cell metastasis. We observed that abundance glycosphingolipids (GSLs), especially the gangliosides subtype, strikingly decreased during the TGF-β-induced EMT of mouse NMuMG cells and human lung A549 adenocarcinoma cells. Transcriptional profiling showed that the TGF-β/SMAD response genes and EMT signatures are strongly enriched in NMuMG cells depleted of UDP-glucose ceramide glucosyltransferase (Ugcg), which catalyses the initial step in GSL biosynthesis. Consistent with this notion, the genetic or pharmacological inhibition of UGCG promoted TGF-β signalling and TGF-β-induced EMT. The inhibition of UGCG stimulated A549 cell migration and extravasation in the zebrafish xenograft model. Mechanistically, GSLs inhibited TGF-β signalling by promoting the TGF-β type I receptor (TβRI) localisation into lipid rafts and by increasing TβRI ubiquitination and degradation. Importantly, we identified ST3GAL5-synthesised *a*-series gangliosides as the main branch of GSLs involved in the inhibition of TGF-β signalling and TGF-β-induced EMT in A549 cells. Notably, ST3GAL5 is weakly expressed in lung cancer tissues compared to adjacent normal tissues, and its expression correlated with good prognosis.

Introduction

Transforming growth factor beta (TGF-β) is the prototypic member of a multifunctional family of secreted dimeric cytokines containing more than 30 structurally and functionally related proteins, which fulfil essential roles in embryogenesis and controlling tissue homeostasis. TGF-β regulates the proliferation, differentiation, death, migration, and invasion of a multitude of cells in a highly contextual manner [1, 2]. TGF-β initiates signalling by binding to the transmembrane TGF-β type II receptor (TβRII) that is endowed with serine/threonine kinase activity [3, 4]. Thereafter, the TGF-β type I receptor (TβRI) is recruited to form a heteromeric complex with TβRII and becomes trans-phosphorylated by the TβRII kinase [5]. Upon TβRI activation, intracellular signalling continues with the

phosphorylation of the Sma- and Mad-related (SMAD) proteins, i.e., SMAD2 and SMAD3, by the TβRI kinase at the two carboxy-terminal serine residues. These activated R-SMADs form heteromeric complexes with a common SMAD mediator, i.e., SMAD4 [6]. Subsequently, these activated SMAD complexes translocate into the nucleus, where they interact with high-affinity DNA binding transcription factors and chromatin remodelling proteins to modulate the transcription of target genes such as *SMAD7*, *SERPINE1*, *CCN2*, encoding SMAD7, PAI1, and CTGF proteins, respectively [7, 8].

Every step of the TGF-β signalling pathway is precisely controlled and subjected to crosstalk with other signalling pathways. One key step in which TGF-β signalling intensity and duration is determined is by the endocytosis and intracellular sorting of cell surface TGF-β receptors [9]. Two major endocytic pathways regulate the internalisation of TGF-β receptors, which are clathrin-mediated and lipid-raft- or caveolae-mediated endocytosis. Clathrin-dependent endocytosis is based on directing TGF-β receptors to the early endosomes enriched for the early endosomal antigen 1 (EEA1) and the SMAD anchor for receptor activation protein (SARA) [10]. After entering the early endosomes, TGF-β receptors associate with FYVE domain-containing protein SARA, resulting in the enhancement of TGF-β-induced SMAD2/3 complex activation and the subsequent propagation of SMAD-dependent signalling [11]. The internalised receptors can be sorted to recycling endosomes in order to return back to the membrane in a Rab11-dependent manner [12]. For the lipid-raft-mediated internalisation, the TGF-β receptors enter caveolin-positive vesicles, where the TβRI preferentially associates with SMAD7 [13]. SMAD7, a negatively regulator of TGFβ signalling, competes with SMAD2/3 for interaction with TβRI or recruits E3 ubiquitin ligases such as SMAD-specific E3 ubiquitin protein ligase 1/2 (SMURF1/2) for the ubiquitin-dependent lysosomal degradation of the TGFβ receptor complex, among other negative regulatory mechanisms [14, 15]. Therefore, the clathrin-mediated endocytosis of TGF-β receptors promotes TGF-β/SMAD signalling, whereas the internalisation mediated by caveolin terminates signalling.

The epithelial-mesenchymal transition (EMT) is a dynamic and reversible morphological process in which the epithelial cells lose their cell–cell contacts and apical–basal polarity, to gain mesenchymal phenotypes with enhanced cell motility [16]. EMT can be characterised by a decreased expression in epithelial markers, i.e., E-cadherin and β-catenin, and a gain in the expression of mesenchymal markers, i.e., N-cadherin, vimentin, SNAIL1/2, and ZEB [17]. The transition state from epithelial to mesenchymal is often incomplete, and the intermediate states display mixed E/M characteristics. This process is referred to as epithelial-mesenchymal plasticity (EMP) [18]. EMT is a transient and reversible critical process during embryonic development [19] and wound healing [20]. Moreover, it plays an important role in pathological processes, specifically in cancer progression and fibrosis [21, 22]. TGF-β is a potent inducer of EMT [23]. However, how dynamic TGF-β receptor signalling pathways control EMT and how this process is precisely regulated and executed and contributes to cancer progression is not well understood.

Glycosylation involves the addition of sugars to proteins and lipids catalysed by various enzymes including glycosyltransferases [24]. Protein glycosylation mainly involves the attachment of *N*-linked glycans (*N*-glycans), *O*-linked glycans (*O*-glycans), glycosaminoglycans (GAG), or glycosylphosphatidylinositol (GPI) anchors to peptide backbones [25]. Glycosphingolipids (GSLs) are the major class of glycolipids found in the cell membranes. The biosynthesis of GSLs is a stepwise process starting with ceramide getting galactosylated to form galactosylceramide (GalCer) or glucosylated by the specific enzyme UDP-glucose ceramide glucosyltransferase (UGCG) to form glucosylceramide (GlcCer) [26]. Subsequently, GlcCer is elongated by the addition of Gal, which is catalysed by enzymes B4GALT5/6 to form lactosylceramide (LacCer), which is the precursor for the formation of three GSL classes gangliosides, (iso-)globosides, and (neo-)lacto-series GSLs [26]. GSLs, together with cholesterol and selected proteins, including GPI-anchored proteins and some transmembrane signalling proteins such as receptor tyrosine kinases, are enriched in cellular membrane microdomains, so-called lipid rafts [27]. The GSL-mediated formation of lipid rafts may affect the localisation of signalling molecules and thereby modulate the cellular signalling

responses. Indeed, several growth factor receptors including the epidermal growth factor (EGF) receptor, the insulin receptor, and the nerve growth factor receptor are localised in membrane microdomains, and their signalling functions have been reported to be modulated by glycolipids [28-31]. Previous studies have shown that the aberrant expression of certain glycosyltransferases in the synthesis of *N*- and *O*- glycans often affects TGF-β signalling and can be involved in TGF-β-induced EMT [32, 33]. Although changes in GSLs during the EMT process have been reported [34], whether there is a functional link between GSLs and TGF-β signalling or TGF-β-induced EMT has remained unclear. In part, this can be attributed to the insufficient sensitivity and analytical depth of methodologies for GSL analysis used in previous studies.

In this study, we used two *in vitro* EMT model cell systems, i.e., mouse normal mammary gland epithelial NMuMG cells and human lung epithelial adenocarcinoma A549 cells, to investigate the alterations and role of GSLs in TGF-β-induced EMT using our highly sensitive analytical platform. Our study showed a strong decrease in GSLs in these two cells undergoing TGF-β-induced EMT. Furthermore, the inhibition of GSL expression by the inactivation of glycosyltransferase UGCG promoted TGF-β signalling and TGF-β-induced EMT using *in vitro* and *in vivo* models. Importantly, ST3GAL5, which catalyses the synthesis of a-series of gangliosides, inhibited TGF-β signalling responses. These gangliosides were found to determine TβRI localisation in lipid rafts and control TβRI ubiquitination and turnover. Strikingly, we found that ST3GAL5 is expressed at much lower levels in lung cancer tissues than adjacent normal tissues, and its expression correlated with good prognosis of lung cancer patients.

Results

TGF-β inhibits the expression of gangliosides in NMuMG and A549-VIM-RFP cell lines

To investigate the TGF-β-induced changes of GSL-glycans in cells undergoing EMT, we chose two established cell models with prominent TGF-β-induced EMT responses, i.e., NMuMG [35] and A549-vimentin

(VIM)-red fluorescent protein (RFP) cell lines [36]. We performed a quantitative glycomic analysis of these cell lines using porous graphitised carbon (PGC) nano-liquid chromatography-electrospray tandem mass spectrometry (nano-LC-ESI-MS/MS) in negative electrospray ionisation mode allowing an in-depth determination of the GSL profile, powerful isomeric separation, and a structural characterisation (Appendix Figure S1) [37]. The high separation power of PGC chromatography enables the discrimination between glycan linkages and positional isomers [37, 38]. Identification of GSL-glycans was performed based on PGC retention time, the known MS/MS fragmentation patterns, described biosynthetic pathways and manual inspection of the fragmentation spectra. All annotated structures with relative abundance are listed in Appendix Table S1. MS/MS peak lists with glycan annotations per cell line are available via an online repository Unicarb DR (https ://unica rb-dr.biomedicin e.gu.se/) [39]. In addition to relative quantification, we also spiked GT1b as an internal standard to monitor the expression level of GSL-glycans. With this approach, we were able to provide a full profile of GSL present on the cell membrane, to identify the most abundant glycans representing more than 98% of the relative intensity, and to quantify the expression of GSLs during TGF-β-induced EMT responses in two cell models (Appendix Figure S2A). The most abundant GSLs that were found in non-treated NMuMG cells were gangliosides, including *o*-, *a*-, and *b*-series, along with a small amount of globoside iGb3 neo-expressed after TGF-β treatment (Appendix Figure S2A). Although the relative abundance of all the individual gangliosides remained unaffected by TGF-β treatment for 48 h (Appendix Figure S2B), the absolute quantities of these gangliosides, especially GM3, GM2, GM1a, GM1b, GD1a, Gg4, GalNAc-GD1a, and GD1a-NeuGc, were significantly decreased (Figure 1A, 1B). In parallel, the same glycosylation analysis was performed in A549-VIM-RFP cells (Appendix Figure S3A). We observed a GSL-glycan profile similar to that obtained with NMuMG cells. Besides the highly expressed *a*- and *b*-series of gangliosides, a small amount of (iso)globosides, i.e., Gb3 and Gb4, and (neo)lacto-series GSLs, i.e., Lc3, nLc4, and sialylated nLc4 (S(3)nLc4), were detected in non-treated A549-VIM-RFP cells (Appendix Figure S3A). Similar to NMuMG, a strong decrease in GSLs in absolute abundance, including GM3, GM2, GM1, and GD3, was observed in TGF-

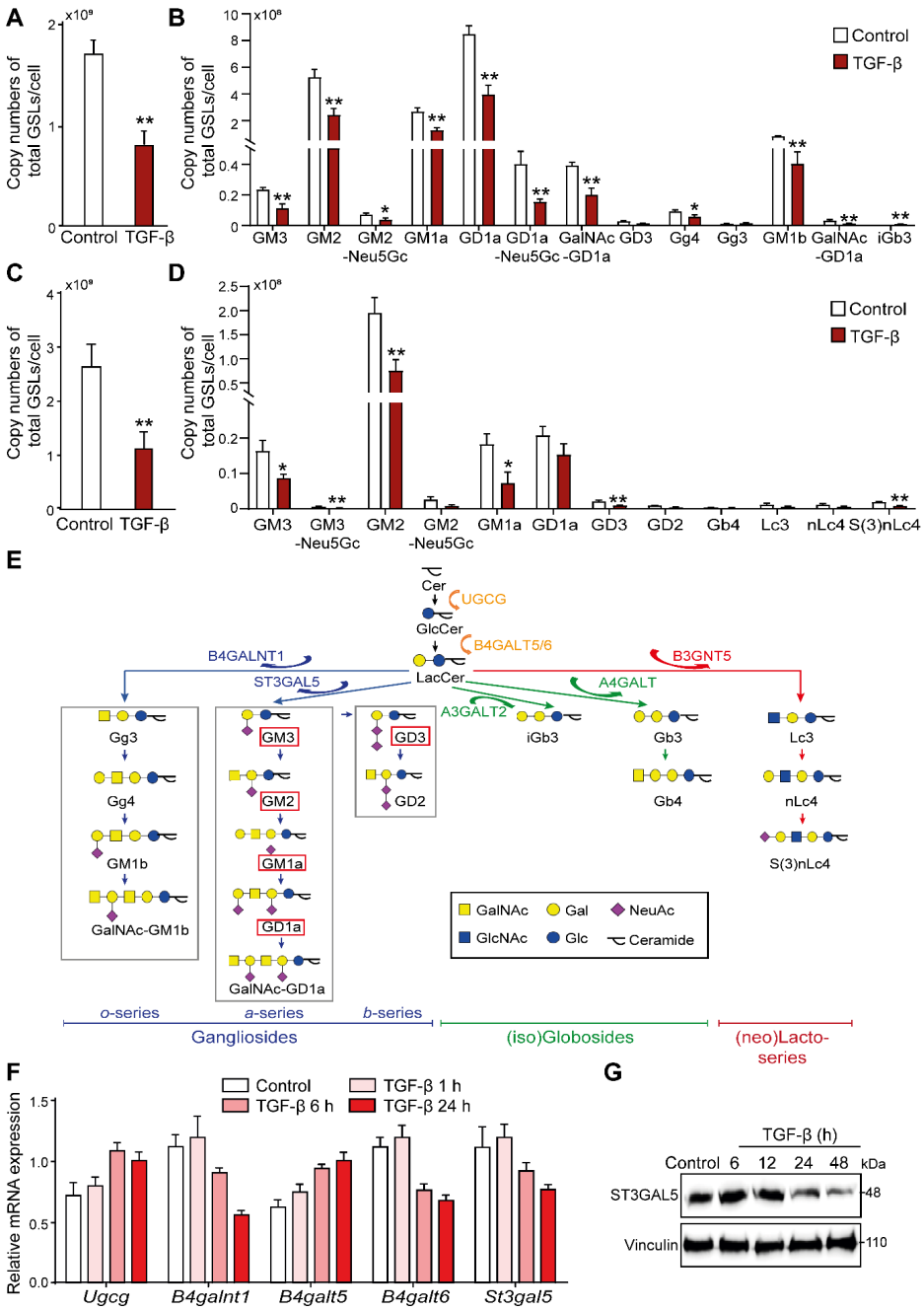

Figure 1. TGF-β decreases the abundance of glycosphingolipid (GSL)-glycans. Average copy numbers of **(A)** total GSL-glycans **(B)** individual GSL-glycans per cell in NMuMG cells with TGF-β stimulation. Average copy numbers of **(C)** total GSL-glycans **(D)** individual GSL-glycans per cell in A549-VIM-RFP cells treated with TGF-β. **(E)**

GSL biosynthesis scheme. GSLs presented in both NMuMG cells and A549-VIM-RFP cells are highlighted by red boxes. **(F)** qRT-PCR analysis of GSL-related gene expression in NMuMG cells after treatment with vehicle control or TGF-β for 1, 6, or 24 h. Histograms provide mean ± SEM, n=3. **(G)** Immunoblot of ST3GAL5 in NMuMG cells treated with vehicle control or TGF-β for the indicated time. Vinculin: loading control. If not stated otherwise, TGF-β (2.5 ng/mL) and the vehicle control were applied for 48 h. Histograms provide mean ± SD, n=3. *, $P \leq 0.05$, **, $p < 0.01$, based on an unpaired Student's t-test. GT1b: internal standard for normalization.

β-stimulated A549-VIM-RFP cells compared to control groups (Figure 1C, 1D). Most of the GSLs, such as GM3, GM1a, GD3, GD2, and Gb4, showed no significant change in relative quantification, except for the slightly decreased GM2 and increased GD1a (Appendix Figure S3B). Figure 1E summarises the GSL biosynthetic pathways and basal GSL expression pattern in the NMuMG and A549-VIM-RFP cell lines; GSL types that are present in both cell lines are highly similar. In line with the glycomic profiling, the gene expression levels of B4galnt1, B5galt6, and St3gal5, which are essential enzymes to catalyse the formation of gangliosides, also decreased upon TGF-β treatment in NMuMG cells (Figure 1F). Furthermore, TGF-β inhibited the ST3GAL5 protein levels in a time-dependent manner in NMuMG cells (Figure 1G).

UGCG knockout leads to the promotion of TGF-β signalling and TGF-β-induced EMT in NMuMG cells

The synthesis of GSLs starts with the addition of glucose to a ceramide and follows with the formation of more complex GSL structures catalysed by specific glycosylation-related enzymes. Glycosyltransferase UGCG is the first enzyme to initiate this biosynthesis pathway [40]. To investigate the role of GSLs in TGF-β signalling, we generated the *Ugcg* NMuMG knockout (KO) cells by clustered regularly interspaced short palindromic repeats (CRISPR)-associated protein 9 (Cas9) gene editing and picked up two KO independent single cell clones. The depletion of *Ugcg* and its GSL products were confirmed by various functional experiments.

We performed a UGCG enzymatic activity assay by incubating the cell lysates of control (expressing Cas9) or KO cells with a BODIPY-conjugated analogue of the UGCG substrate ceramide, followed by thin layer chromatography (TLC) of extracted GSLs (Figure EV1A). The data showed a near absence of BODIPY-GlcCer in the lysates of *Ugcg* KO

cells, demonstrating the high knockout efficiency. By using the Alexa-488 fluorophore-conjugated cholera toxin subunit B (CTB) and fluorescent activated cell sorting (FACS) analysis, we detected a significant decrease in GM1, a subtype of gangliosides that interacts with CTB, in *Ugcg* KO NMuMG cells (Figure EV1B). Similarly, according to the glycomic profiling results and the quantification of the absolute abundance of individual GSLs, all GSLs were depleted in *Ugcg* KO cells (Figure 2A, Figure EV1C, EV1D).

Next, to obtain insight in signalling pathways and processes affected upon UGCG depletion, we compared the transcriptional profiles in NMuMG cells without or with *Ugcg* KO by RNA sequencing (RNA-seq) and performed gene set enrichment analysis (GSEA). Importantly, we observed that a mouse TGF-β gene response signature (consisting of 109 genes) was significantly enriched in UGCG-depleted NMuMG cells, indicating the negative correlation between UGCG and TGF-β signalling (Figure 2B). The GSEA performed with a human TGF-β gene response signature (containing 189 genes) also showed a similar negative correlation, confirming the notion that UGCG mediates an inhibition of TGF-β signalling (Figure EV1E). In addition, we found that UGCG is also negatively correlated with the EMT process based on GSEA using mouse and human EMT gene signatures (Figure 2C, Figure EV1F). Thereafter, we examined the effect of UGCG depletion on TGF-β-induced responses and EMT marker expression levels in NNuMG cells. Consistent with our RNA profiling results, we observed a significant upregulation of basal and TGF-β-induced p-SMAD2 in UGCG-depleted NMuMG cells (Figure 2D, Figure EV1G). In line with this, qRT-PCR assay confirmed that, upon the loss of UGCG, the expression levels of TGF-β target genes including *SMAD7* and *SERPINE1* (Figure 2E) are elevated. For the TGF-β-induced EMT, the depletion of UGCG inhibited the expression of epithelial marker E-cadherin and promoted the expression of mesenchymal marker N-cadherin both at mRNA and protein levels (Figure 2F, G). The enhanced TGF-β-induced EMT upon *Ugcg* KO was further validated by the decreased E-cadherin expression and more filamentous (F)-actin formation in *Ugcg* KO cells compared to control groups as measured by

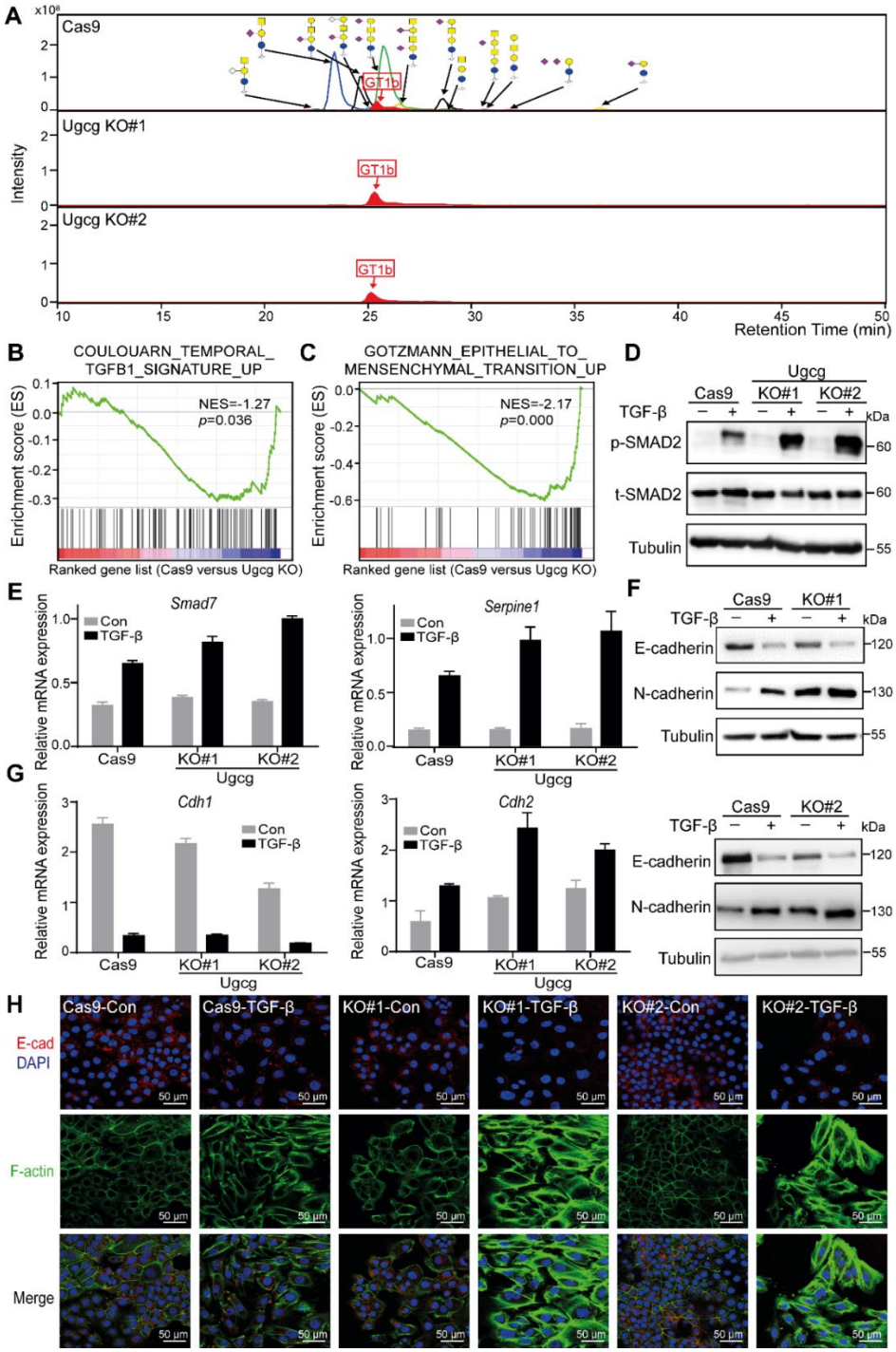

Figure 2. Knockout of Ugcg, a key enzyme in the biosynthesis of GSLs, promotes

TGF-β signalling and TGF-β-induced EMT in NMuMG cells. (A) Combined EIC of GSL-glycans in Ugcg KO cell line and control NMuMG cell line. **(B)** Mouse TGF-β gene signatures are enriched in NMuMG cells with Cas9 versus Ugcg KO shown by gene-set enrichment analysis (GSEA). Normalized Enrichment Score (NES) = -1.27, p = 0.036. **(C)** GSEA of mouse EMT gene signatures in NMuMG cells with Cas9 versus Ugcg KO. NES = -2.17, p = 0.000. **(D)** Immunoblot analysis of p-SMAD2 and total SMAD2 (t-SMAD2) levels in NMuMG cells without or with UGCG deficiency that were treated with vehicle control or TGF-β for 1 h. Tubulin: loading control. **(E)** qRT-PCR analysis of TGF-β target genes, including *Smad7* and *Serpine1*, in Ugcg KO NMuMG cell lines or the control NMuMG cell line treated with vehicle control or TGF-β for 6 h. **(F)** Immunoblot analysis of E-cadherin and N-cadherin in Ugcg KO NMuMG cell lines or the control NMuMG cell line treated with vehicle control or TGF-β for 48 h. Tubulin: loading control. **(G)** Expression of *Cdh1* and *Cdh2* gene levels in NMuMG Ugcg KO cell lines or the control NMuMG cell line after vehicle control or TGF-β treatment for 48 h. **(H)** Immunofluorescence analysis of the expression and localization of E-cadherin (red) and the formation of filamentous (F)-actin (green) after treatment with vehicle control or TGF-β for 2 days. Nuclei were counterstained with DAPI (blue). Images were captured with confocal microscopy. Scale bar = 50 μm. Data information: TGF-β was applied at a final concentration of 2.5 ng/mL. In (E, G), data are expressed as mean ± SD, n=3

immunofluorescent staining of the anti-E-cadherin antibody and FITC-conjugated phalloidin, respectively (Figure 2H).

The activation of EMT can provide cells with an enhanced ability to migrate [35]. We thus further investigated the basal migration rate upon *Ugcg* KO in NMuMG cells. The NMuMG cells with UGCG depletion showed enhanced migration compared to control cells (Figure EV1H, EV1I). Taken together, these results show that UGCG is a critical inhibitor of TGF-β/SMAD signalling and EMT in NMuMG cells.

Eliglustat, an UGCG activity inhibitor, promotes TGF-β signalling, TGF-β-induced EMT, cell migration, and invasion

Having determined the inhibitory role of UGCG on TGF-β signalling and EMT in mouse normal epithelial NMuMG cells, we expanded our study to human lung cancer A549 cells. To inactivate UGCG glucosylceramide synthase activity, we used the clinically approved GSL synthesis inhibitor eliglustat [41]. The effectiveness of eliglustat as UGCG inhibitor was confirmed by measuring GM1 expression using FACS analysis (Figure EV2A, EV2B). Eliglustat treatment strongly promoted TGF-β-induced p-SMAD2 phosphorylation in A549-VIM-RFP cells (Figure 3A, 3B, EV2C).

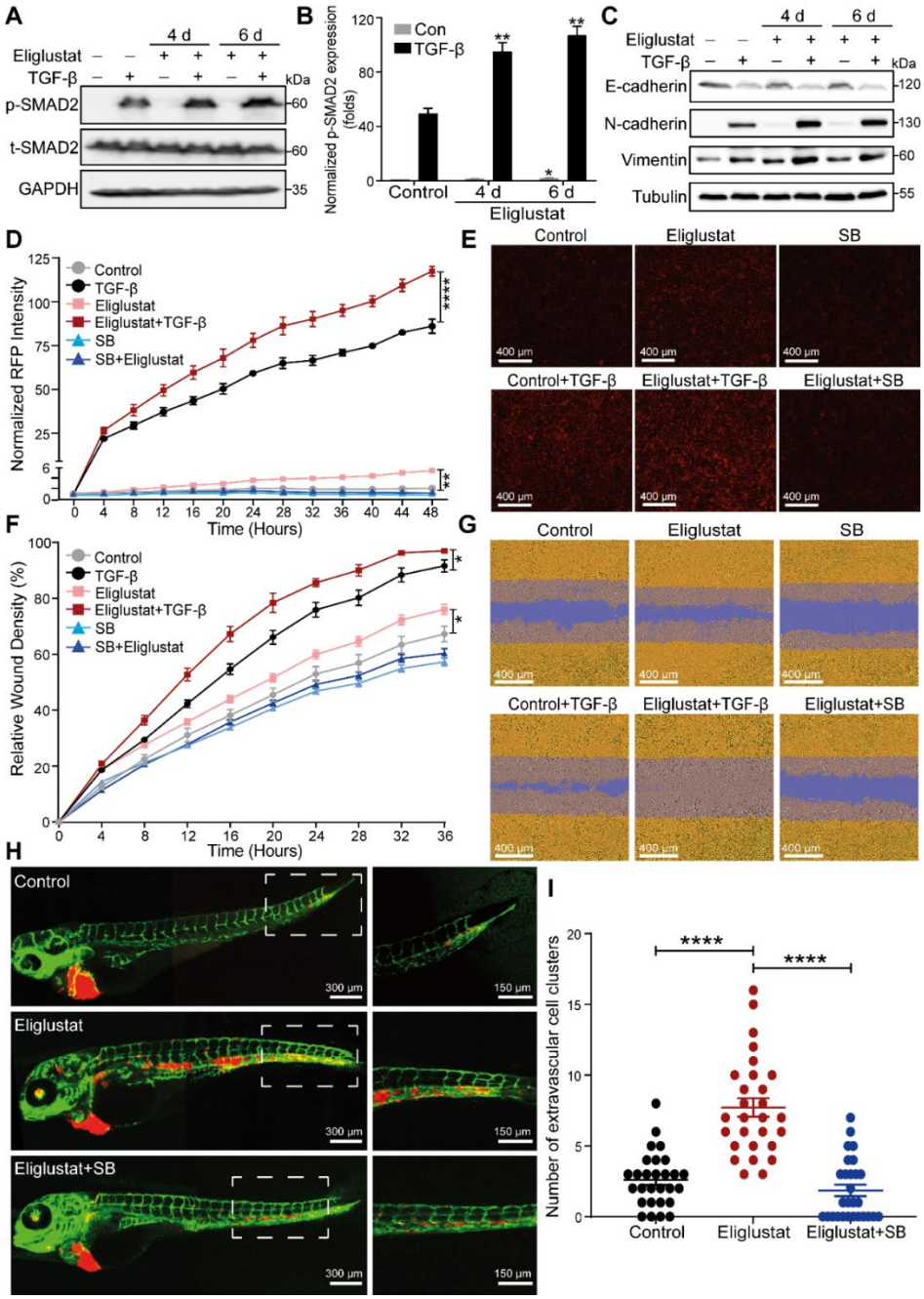

Figure 3. Eliglustat, an UGCG inhibitor, enhances TGF-β signalling and TGF-β-induced EMT, cell migration and invasion in A549 cells. (A) Immunoblot analysis of

p-SMAD, t-SMAD2 expression levels of A549-VIM-RFP cells that were pretreated with eliglustat for 4 or 6 days and then treated with vehicle control or TGF-β for 1 h. GAPDH: loading control. **(B)** Quantification of p-SMAD2 expression in A549-VIM-RFP cells including control groups (with or without TGF-β) and 4- and 6-day eliglustat treatment groups (with or without TGF-β). Results were normalized by the expression of GAPDH, and fold changes were then further normalized by the expression of p-SMAD2 in the control group without TGF-β treatment. **(C)** Immunoblot analysis of epithelial marker, E-cadherin, and mesenchymal markers including N-cadherin and vimentin expression levels in A549-VIM-RFP cells that were treated with eliglustat for 4 or 6 days and/or vehicle control and/or TGF-β for 2 days. Tubulin: loading control. **(D)** Effect of eliglustat (pre-)treatment for 4 days on vimentin expression in A549-VIM-RFP cells in response to TGF-β and/or SB505124 (SB, 1 μM) for the indicated times. Time course for the expression of RFP-conjugated vimentin was measured by IncuCyte. Red object intensity was normalized by the red intensity at 0 h. **(E)** Representative images of RFP-vimentin expression at the end time point (48 h) in the control group and the eliglustat- and SB505124-treated groups combined with vehicle control or TGF-β in A549-VIM-RFP cells. Scale bar = 400 μm. **(F)** A549-VIM-RFP cells were pretreated with eliglustat for 4 days and then incubated with TGF-β or SB505124 (SB, 1 μM) for the indicated times. Real-time scratch assay results were analyzed by IncuCyte. **(G)** Representative images of a scratch wound at the end time point (36 h) in the control group and the eliglustat-treated groups combined with vehicle control or TGF-β or SB505124 in A549-VIM-RFP cells. The region of the original scratch is indicated in purple, and the area of the cell is colored in yellow. **(H)** mCherry-labelled A549 cells were pretreated with eliglustat (2 μM) for 4 days and thereafter injected into ducts of Cuvier of zebrafish embryos. Representative images with zoom-in pictures (outlined with a dotted square) of extravasated cells were captured 4 days after injection by confocal microscope. SB groups zebrafish were treated with a 1 μM SB505124 inhibitor in the egg water together with eliglustat for 4 days after injection and refreshed every day. Scale bar = 300 μm or 150 μm. **(I)** Quantification of the number of extravasated cell clusters from 28 embryos for each group. ****, $P < 0.0001$, based on an unpaired Student's t-test, n=2. Data information: TGF-β and eliglustat were applied at a final concentration of 2.5 ng/mL and 2 μM, respectively. In (B, D, F), data are expressed as mean ± SEM, n=3. *, $P \leq 0.05$, **, $P < 0.01$, ****, $P < 0.0001$, based on an unpaired Student's t-test.

Moreover, the addition of eliglustat inhibited the expression of epithelial marker E-cadherin and enhanced the expression of mesenchymal markers, including N-cadherin and vimentin, in the absence or presence of exogenous TGF-β (Figure 3C). The eliglustat-mediated promotion of TGF-β-induced EMT was further confirmed by the dynamic increase in RFP-tagged vimentin (Figure 3D, 3E). We next investigated whether this UGCG inhibitor promotes the migration and invasion abilities of A549-VIM-RFP cells. As expected, using a scratch assay, eliglustat treatment

enhanced both basal and TGF-β-induced cell migration (Figure 3F, 3G). The eliglustat-induced promotion of cell migration was completely blocked by the addition of the highly selective small molecule TβRI kinase inhibitor SB505124. The latter indicates that the eliglustat-induced cell migration requires TβRI signalling (Figure 3F, 3G). Next, we investigated the effect of eliglustat on the extravasation of A549 cells using a zebrafish xenograft model system. We pretreated the mCherry-labelled A549 cells with eliglustat for four days and thereafter injected them into the ducts of Cuvier of embryonic zebrafish. The number of extravascular cell clusters were examined four days after injection. Eliglustat-treated cells/embryos exhibited a stronger invasive capability when compared to the non-treated cells/embryos (Figure 3H, 3I). Furthermore, SB505124 significantly blocked the eliglustat-induced extravasation of A549 cell extravasation (Figure 3H, 3I). We also examined the inhibitory effect of eliglustat on the GSLs biosynthesis in NMuMG cells by FACS (Figure EV2D). Similar to A549 cells, we observed, after eliglustat addition, a (slight) enhancement in TGF-β/SMAD2 signalling and TGF-β-induced EMT (Figure EV2E, EV2F). Taken together, these data demonstrate that UGCG and UGCG-defined GSLs inhibit TGF-β signalling and EMT in mouse epithelial NMuMG cells and human lung cancer A549 cells, as well as in cell migration and the extravasation of A549 cells.

Inhibition of GSL biosynthesis decreases the localisation of TβRI in lipid rafts and protects TβRI from ubiquitination and increases its stability

GSLs were found to impact signal transduction pathways by regulating the internalization of cell surface proteins. They can do so by facilitating the lateral interaction between membrane-anchored molecules, such as transmembrane protein receptors, in lipid rafts or caveolae membranes [42-45]. However, how GSLs control TGF-β receptor signalling and TGF-β-receptor-induced EMT is not well understood. Therefore, we investigated whether the inhibition of GSL synthesis can affect the partition of TβRI between lipid raft and non-lipid raft microdomains in the plasma membrane. We performed a sucrose density gradient ultracentrifugation analysis to isolate the raft and non-raft fractions in *Ugcg* KO NMuMG cells or A549-VIM-RFP cells treated with the UGCG

inhibitor eliglustat. The distinctive distribution of specific lipid raft marker flotillin-1 and non-raft markers including β1-integrin and EEA1 in non-raft fractions indicated the successful isolation of fractions containing lipid raft and non-lipid raft microdomains (Figure 4A, 4C). UGCG depletion led to the decrease in lipid raft microdomains, which resulted in a decreased level of TβRI in raft-containing fractions (Fractions 3-5) in *Ugcg* KO cells compared to the control NMuMG cells (Figure 4A, 4B).

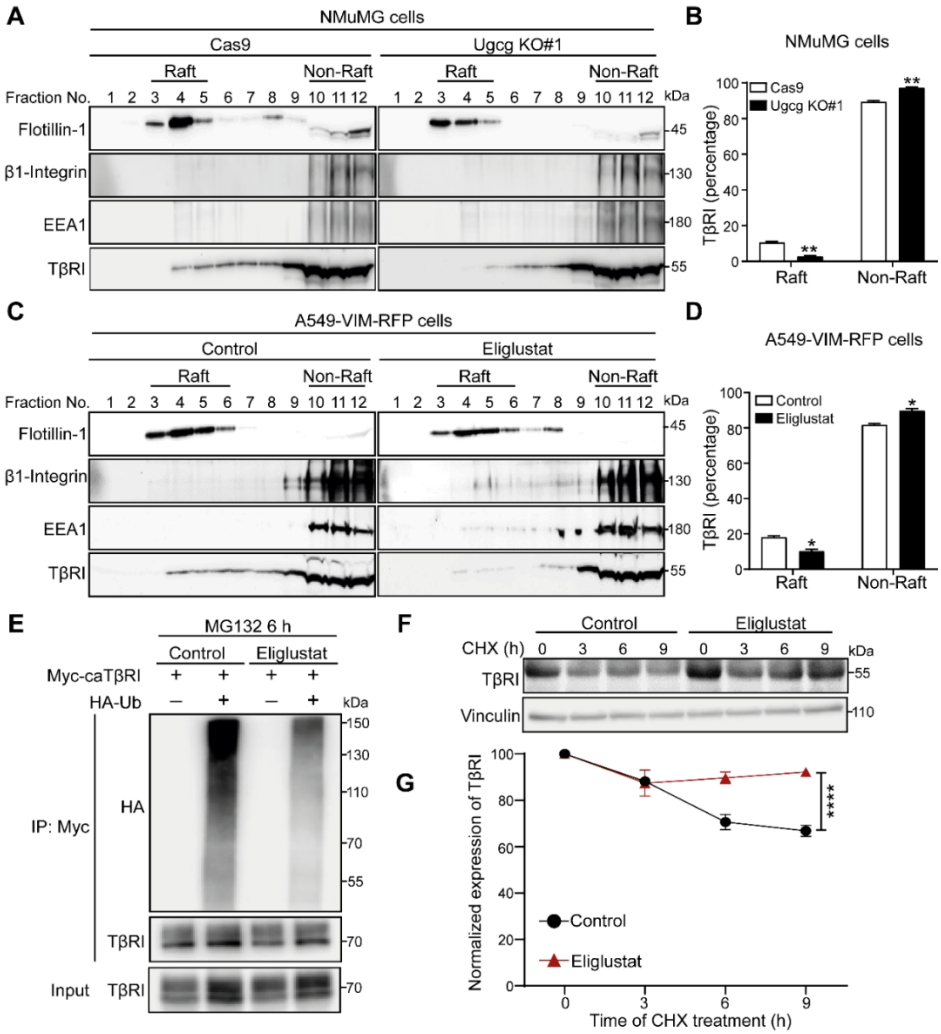

Figure 4. Inhibition of GSL biosynthesis decreases the TβRI level in lipid rafts and inhibits the ubiquitination and degradation of TβRI. (A) Cell lysates from NMuMG control cells (Cas9-expressing cells) or Ugcg KO cells were subjected to sucrose density gradient ultracentrifugation. The expression levels of flotillin-1, β1-integrin, EEA1, and

TβRI in sucrose gradient fractions were analyzed by immunoblot analysis. Fractions 3, 4, and 5 contained lipid rafts, whereas Fractions 10-12 corresponded to non-lipid raft fractions. **(B)** Quantification of TβRI percentages in lipid rafts and non-lipid raft fractions in Ugcg KO NMuMG and control cells. **(C)** Isolation of lipid rafts from other cellular components in A549-VIM-RFP cells treated with UGCG inhibitor eliglustat (2 μM) for 6 days using sucrose density gradient ultracentrifugation and the detection of flotillin-1, β1-integrin, EEA1, and TβRI levels in sucrose gradient fractions using immunoblot analysis. Fractions 3-6 contained lipid rafts, whereas Fractions 10–12 corresponded to the non-lipid raft fractions. **(D)** Quantification of TβRI percentages in lipid raft and non-lipid raft fractions in A549-VIM-RFP cells treated with eliglustat (2 μM) for 6 days. **(E)** Ubiquitination of TβRI was detected by IP of Myc-tagged constitutively active TβRI (caTβRI) from HA-Ubiquitin (HA-Ub) transfected HEK293T cells with or without eliglustat (2 μM) treatment for 6 days. All groups were treated with MG132 (5 μM) for 6 h. **(F)** Immunoblot analysis of TβRI expression levels in the control group or eliglustat (2 μM) treated A549-VIM-RFP cells with 50 μg/mL cycloheximide (CHX) treatment for the indicated times. Vinculin: loading control. **(G)** Quantification of the TβRI expression levels normalized to the t=0 controls. In (B, D), data are expressed as mean ± SEM, n=2. In (G), data are expressed as mean ± SEM, n=3. *, $P \leq 0.05$, **, $P < 0.01$, ****, $P < 0.0001$, based on an unpaired Student's t-test.

In line with this, the inhibition of GSL biosynthesis in A549-VIM-RFP cells by the UGCG inhibitor eliglustat also decreased the TβRI levels in lipid raft fractions (Fractions 3-6) (Figure 4C, 4D). Furthermore, we examined the effects of eliglustat on the ubiquitination of TβRI by overexpressing Myc-tagged constitutively active TβRI (caTβRI) and HA-tagged ubiquitin in human embryonic kidney (HEK) 293T cells. UGCG inhibitor eliglustat mitigated caTβRI ubiquitination in the presence of the proteasome inhibitor MG132 (Figure 4E). The role of eliglustat on regulating the stability of TβRI was studied by examining TβRI expression after treatment with the protein synthesis inhibitor cycloheximide (CHX) in A549 cells. The protein half-lives of TβRI were prolonged by eliglustat treatment (Figure 4F, 4G). Taken together, these results suggest that the underlying mechanism for the GSL depletion-induced inhibition of TGF-β signalling is caused by favoring a localisation of TβRI on lipid rafts, thereby triggering its ubiquitination and subsequent degradation.

ST3GAL5-mediated biosynthesis of *a*-series gangliosides inhibits TGF-β signalling and TGF-β-induced EMT and induces the ubiquitination and degradation of TβRI

After showing the inhibitory effects of GSLs on TGF-β signalling and TGF-β-induced EMT, we set out to elucidate the specific enzyme(s) involved in the biosynthesis of GSLs that were found to be decreased in response to TGF-β challenge. Since ~95% of GSLs decreased by TGF-β stimulation in A549-VIM-RFP cells were gangliosides, we focused our studies on the two critical enzymes B4GALNT1 and ST3GAL5, which catalyse the synthesis of *o*-series and *a* or *b*-series gangliosides, respectively. To investigate their functional involvement, we generated *B4GALNT1*- or *ST3GAL5*-depleted A549 cells using siRNA-mediated transfection. The high efficiency of *ST3GAL5* and *B4GALNT1* knockdown was validated using qRT-PCR analysis (Figure EV3A, EV3B). Glycomic profiling analysis of cells deficient in *ST3GAL5* or *B4GALNT1* using PGC nano-LC-ESI-MS/MS confirmed the strong decrease in specific ganglioside products produced by these two enzymes (Figure 5A, Figure EV3C). ST3GAL5 knockdown showed a significant decrease in GM3, GM2, and GM1a (Figure EV3D, EV3E), which aligns with post TGF-β treatment. *B4GALNT1* knockdown, however, induced a downregulation of total GSLs (Figure EV3D) and led to an increase in GM3 (Figure EV3E). This response is very different to the TGF-β-induced effect on ganglioside levels.

Next, we investigated the effect of ST3GAL5 or B4GALNT1 knockdown on TGF-β signalling and EMT in A549 cells. We found that the depletion of ST3GAL5 enhanced TGF-β-induced SMAD2 phosphorylation (Figure 5B, 5C), whilst B4GALNT1 knockdown had no significant effect (Figure EV4A). Knockdown of ST3GAL5, but not B4GALNT1, enhanced the TGF-β-induced decrease in epithelial marker E-cadherin and increase in mesenchymal markers, i.e., N-cadherin, vimentin, and SNAIL (Figure 5D, Figure EV4B). This was further confirmed by the increase in TGF-β-induced RFP-conjugated vimentin expression upon ST3GAL5 depletion

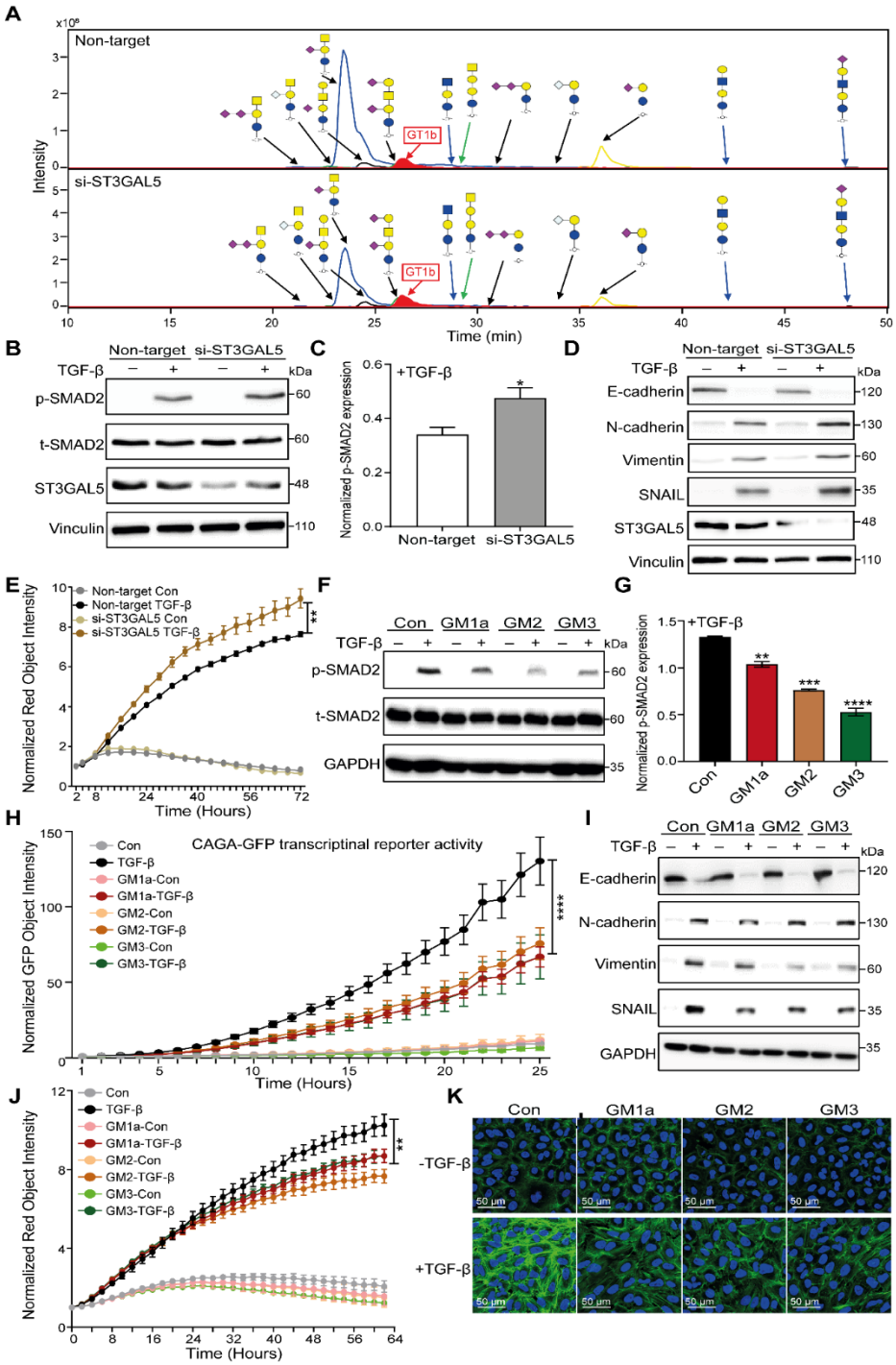

Figure 5. ST3GAL5 and its downstream products including GM3, GM2, and GM1a

inhibit TGF-β signalling and TGF-β-induced EMT. (A) EIC of GSL-glycans released from A549-VIM-RFP cells transfected with non-target, ST3GAL5 or B4GALNT1 siRNAs. GT1b was used as an internal standard for normalization. **(B)** Immunoblot analysis of p-SMAD2, t-SMAD2, and ST3GAL5 in A549-VIM-RFP cells with ST3GAL5 knockdown and non-target siRNA treated with vehicle control or TGF-β for 1 h. Vinculin: loading control. **(C)** Quantification of p-SMAD2 expression in A549-VIM-RFP cells with non-target and ST3GAL5 siRNA treated with TGF-β. **(D)** Expression levels of ST3GAL5, the epithelial marker E-cadherin, and mesenchymal markers including N-cadherin, vimentin, and SNAIL in ST3GAL5-depleted and non-target siRNA-transfected A549-VIM-RFP cells that were treated with vehicle control or TGF-β for 48 h. Vinculin: loading control. **(E)** Time course for the expression of RFP-conjugated vimentin measured by IncuCyte in ST3GAL5 knockdown and non-target siRNA-transfected A549-VIM-RFP cells that were treated with vehicle control or TGF-β for the indicated times. Red object intensity was normalized by the red intensity at 0 h. **(F)** A549-VIM-RFP cells were preincubated 50 μg/mL GM1a, GM2, or GM3 for 24 h and then combined with vehicle control or TGF-β for 1 h, followed by immunoblot analysis of p-SMAD2 and t-SMAD2 expression levels. GAPDH: loading control. **(G)** Quantification of p-SMAD2 expression in A549-VIM-RFP cells treated with 50 μg/mL GM1a, GM2, or GM3 and combined with TGF-β. **(H)** A549-VIM-RFP cells infected with CAGA-GFP lentivirus were pre-treated with 50 μg/mL GM1a, GM2, or GM3 for 24 h and then combined with vehicle control or TGF-β for the indicated times. SMAD3/SMAD4-dependent $(CAGA)_{12}$-mediated transcriptional GFP reporter expression levels were measured by IncuCyte. **(I)** Expression levels of the epithelial marker E-cadherin and mesenchymal markers including N-cadherin, vimentin, and SNAIL in A549-VIM-RFP cells preincubated with 50 μg/mL GM1a, GM2, or GM3 for 24 h and combination with vehicle control or TGF-β for another 48 h by immunoblot analysis. GAPDH: loading control. **(J)** A549-VIM-RFP cells were pre-treated with 50 μg/mL GM1a, GM2, or GM3 for 24 h and then incubated with vehicle control or TGF-β (2.5 ng/mL) for the indicated times. Real-time expression of RFP-conjugated vimentin was measured by IncuCyte, and red object intensity was normalized by the red intensity at 0 h. **(K)** Alexa-488 phalloidin staining for F-actin (green) in A549-VIM-RFP cells preincubated with 50 μg/mL GM1a, GM2, or GM3 for 24 h and combination with vehicle control or TGF-β for another 48 h. Nuclei were counterstained with DAPI (blue). Images were captured with confocal microscopy. Scale bar = 50 μm. Data information: TGF-β were applied at a final concentration of 2.5 ng/mL. In (C, E, F, H, J), data are expressed as mean ± SEM, n=3. *, $P \leq 0.05$, **, $P < 0.01$, ***, $P < 0.001$, ****, $P < 0.0001$, based on an unpaired Student's t-test.

in A549-VIM-RFP cells (Figure 5E). All of these results indicate that ST3GAL5, but not B4GALNT, is the key player in TGF-β signalling and TGF-β-induced EMT.

The ST3GAL5 enzyme catalyses the conversion of LacCer into GM3, which is the precursor ganglioside for extension and further branching reactions to produce *a*-type gangliosides, including GM2, GM1a, and GD1a, and *b*-types such as GD3 and GD2 [26]. Both types of gangliosides were found to be highly expressed in NMuMG and A549 cell lines (Figure 1E). Next, we examined the effect of the exogenous addition of individual *a*- or *b*-series gangliosides on TGF-β signalling. In line with our expectation, the addition of exogenous GM1a, GM2, or GM3 caused an inhibition of TGF-β/SMAD2 signalling in A549-VIM-RFP cells (Figure 5F, 5G). However, the exogenous addition of GD3 elicited no effect on this response (Figure EV4C). In line with these results, pre-treatment of A549 cells with GM1a, GM2, or GM3 exhibited a significant inhibition of TGF-β-induced SMAD3-dependent CAGA-GFP reporter activity (Figure 5H), while the GD3-pre-treated cells showed no change compared to control cells (Figure EV4D). Furthermore, the exogenous addition of GM1a, GM2, or GM3 abrogated the TGF-β-induced expression of mesenchymal markers, including N-cadherin, vimentin, and SNAIL (Figure 5I). In line with this, the TGF-β-induced promotion of RFP-vimentin was attenuated by GM1a, GM2, or GM3 addition (Figure 5J). Moreover, upon stimulation with exogenous GM1a, GM2, or GM3, A549-VIM-RFP cells showed less F-actin formation compared to control groups after TGF-β treatment (Figure 5K). In contrast, the exogenously added GD3 affected neither vimentin expression nor F-actin formation in A549-VIM-RFP cells (Figure EV4E, EV4F). These results indicate the pivotal role of ST3GAL5-synthesised *a*-series, but not *b*-series, gangliosides in TGF-β signalling and TGF-β-induced EMT.

We next investigated the mechanism by which ST3GAL5 induces the inhibition of TGF-β signalling. In Myc-tagged caTβRI and HA-ubiquitin overexpressed HEK293T cells, the knockdown of ST3GAL5 (but not B4GALNT1) significantly decreased the ubiquitination of TβRI in the presence of the proteasome inhibitor MG132 (Figure 6A, Appendix Figure S4A). Conversely, the exogenous GM3 enhanced TβRI ubiquitination in HEK293T cells with an overexpression of Myc-caTβRI and HA-ubiquitin (Figure 6B). The GD3-treated HEK293T cells showed no effect on the ubiquitination of TβRI (Appendix Figure S4B). Moreover,

the half-life of TβRI was shortened upon GM3 treatment (Figure 6C, 6D). Taken together, we found that ST3GAL5-catalysed *a*-series gangliosides mitigate TGF-β signalling responses, induce TβRI ubiquitination, and decrease TβRI stability (Figure 6E).

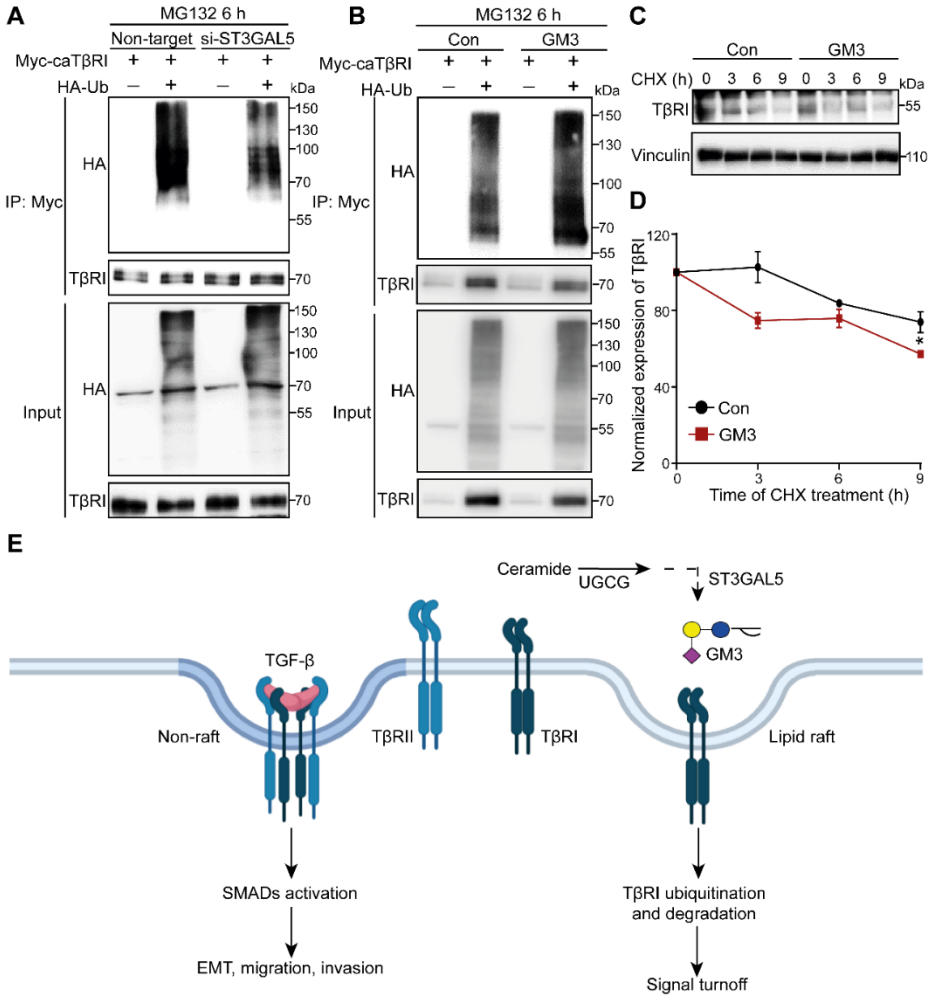

Figure 6. Challenging A549 cells with GM3, a product of ST3GAL5, promotes TβRI ubiquitination and degradation. (A) HEK293T cells transfected with Myc-tagged constitutively active TβRI (caTβRI), HA-Ubiquitin (HA-Ub), and non-target siRNA or ST3GAL5 siRNA were collected for the immunoprecipitation of anti-Myc antibody and immunoblot analysis. All groups were treated with MG132 (5 μM) for 6 h. **(B)** Ubiquitination of TβRI was detected by IP of Myc-tagged caTβRI from HA-Ub transfected HEK293T cells with or without the exogenous addition of GM3 (50 μg/ml) for 24 h. All groups were treated with MG132 (5 μM) for 6 h. **(C)** Western blot analysis

of TβRI expression levels in A549-VIM-RFP cells with or without the exogenous addition of GM3 (50 μg/ml) combined with cycloheximide (CHX) treatment for the indicated times. Vinculin: loading control. **(D)** Quantification of the TβRI expression in the control group or GM3-treated group of A549-VIM-RFP cells. The results were normalized to the t=0 controls. Data are shown as mean ± SEM of three independent experiments. *, $P \leq 0.05$, based on an unpaired Student's t-test. **(E)** Working model for UGCG-ST3GAL5-GM3-mediated inhibition of TGF-β signalling by inducing the localization of TβRI in lipid rafts.

Expression of ST3GAL5 inhibits cell migration and invasion, which is linked to a favorable prognosis of lung cancer

To investigate the function of ST3GAL5 and its catalyzed gangliosides in cell migration, we performed a scratch assay in ST3GAL5 knockdown or control A549 cells. While the depletion of ST3GAL5 promoted the TGF-β-induced migration of A549-VIM-RFP cells (Figure 7A, 7B), the knockdown of B4GALNT1 showed no effect on cell migration compared to non-targeting siRNA-transfected controls (Figure EV5A, EV5B). Moreover, the addition of GM1a, GM2, and GM3, but not GD3, significantly decreased migratory ability upon TGF-β stimulation in A549-VIM-RFP cells (Figure 7C, 7D, EV5C, EV5D). Next, we analysed the effect of the misexpression of ST3GAL5 in lung cancer A549 cells on extravasation in a zebrafish xenograft model. The mCherry-expressing A549 cells with ST3GAL5 depletion were injected into zebrafish embryos, and the number of extravascular clusters were counted four days after injection. In the zebrafish embryo group with injected ST3GAL5 knockdown A549 cells, more cell clusters between blood vessels were observed compared to the zebrafish with non-target siRNA transfected A549 cells (Figure 7E, 7F). This enhanced invasive ability of A549 cells was attenuated by the addition of TβRI inhibitor SB505124. The latter implicates that increased migration upon ST3GAL5 knockdown is, at least in part, caused by increased TβRI signalling (Figure 7E, 7F).

Given the critical role of ST3GAL5 in the regulation of cell migration and invasion, we investigated the possibility that ST3GAL5 might be a relevant biomarker in (early-stage) lung cancer. Using the publicly available cohort of 982 lung cancer patients, we observed that a low expression of ST3GAL5 is associated with a poor prognosis of survival

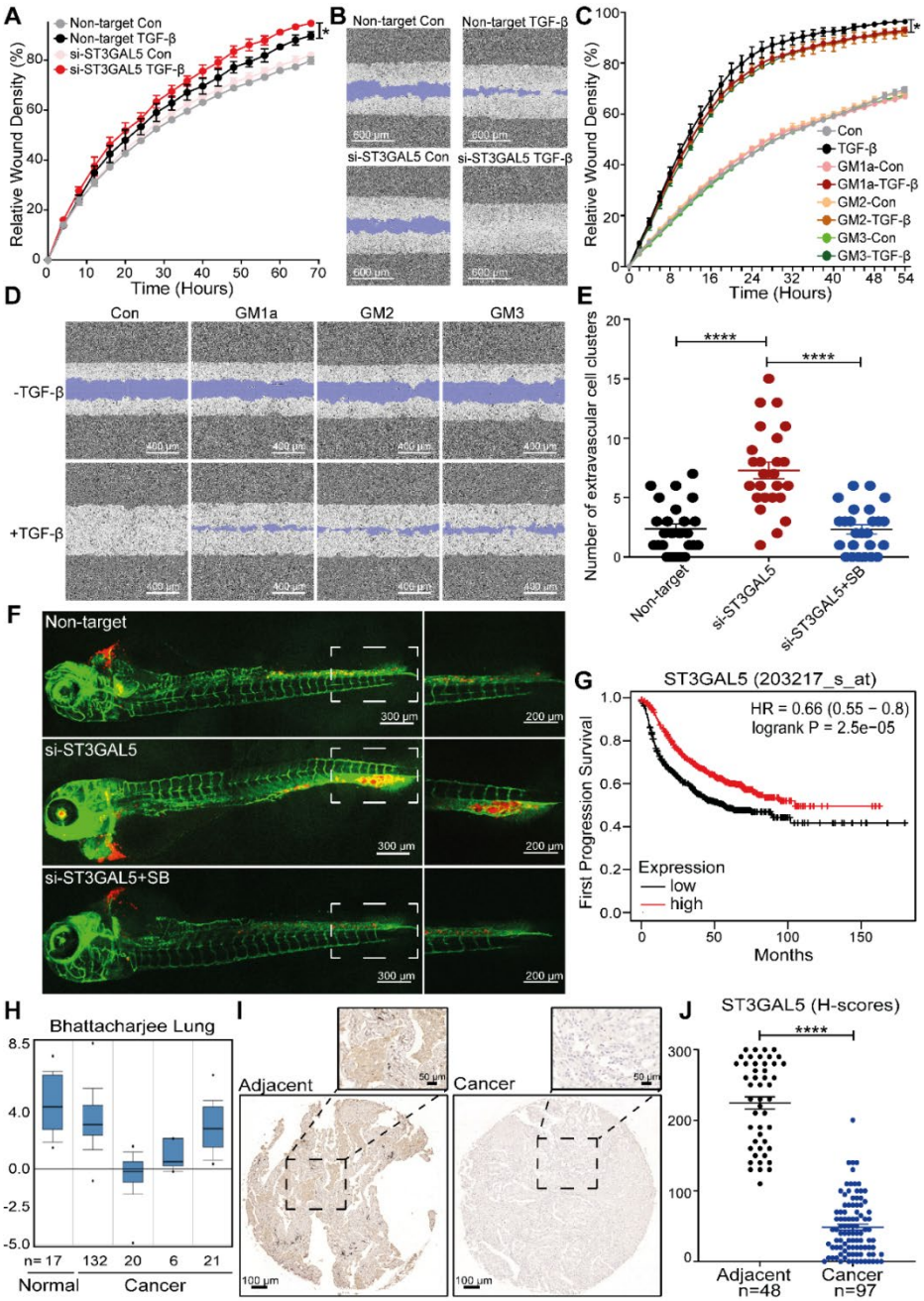

Figure 7. ST3GAL5 inhibits A549 cell migration and invasion, and its expression is associated with good prognosis of lung cancer. (A) Real-time scratch assay results were analyzed by IncuCyte in ST3GAL5 depleted or non-target siRNA-transfected A549-VIM-RFP cells treated with vehicle control or TGF-β (2.5 ng/mL) for the indicated

times. Relative wound density (closure) is presented as the mean ± SEM, n=3. **, P < 0.01, based on an unpaired Student's t-test. **(B)** Representative images of a scratch wound at the end time point (68 h) in the non-target group and ST3GAL5 knockdown group that were treated with vehicle control or TGF-β (2.5 ng/mL) in A549-VIM-RFP cells. The region of the original scratch is indicated in purple. Scale bar = 600 μm. **(C)** A549-VIM-RFP cells were pre-treated with 50 μg/mL GM1a, GM2, or GM3 for 24 h and then incubated with vehicle control or TGF-β (2.5 ng/mL) for the indicated times. Time course for scratch assay results were analyzed by IncuCyte. Relative wound density (closure) was presented as the mean ± SEM, n=3. *, P ⩽ 0.05, based on an unpaired Student's t-test. **(D)** Representative images of a scratch wound at the time point of 50 h in A549-VIM-RFP cells with exogenous addition of 50 μg/mL GM1a, GM2, or GM3 and treatment with vehicle control or TGF-β (2.5 ng/mL). The original scratch region is indicated in purple. Scale bar = 400 μm. **(E)** mCherry-labelled A549 cells with ST3GAL5 depletion or non-target siRNA were injected into ducts of Cuvier of zebrafish embryos. SB zebrafish embryo groups were treated with 1 μM SB505124 inhibitor in the egg water for 4 days after injection and refreshed every day. The number of extravasated cell clusters were quantified from 25 embryos for each group. ****, P < 0.0001, based on an unpaired Student's t-test, n=2. **(F)** Representative images with zoom-in pictures (outlined with a dotted square) of extravasated cells were captured 4 days after injection by confocal microscope. Scale bar = 300 μm or 200 μm. **(G)** Box plots of *ST3GAL5* gene expression levels in lung cancer tissues and normal tissues in the Bhattacharjee Lung database. **(H)** Kaplan–Meier survival curves showing the first progression survival of lung cancer patients in publicly available lung cancer dataset according to *ST3GAL5* expression (n=982). **(I)** Representative images of ST3GAL5 immunohistochemistry in the human lung tissue microarray including normal and cancer tissues. Large field and zoom-in pictures (outlined with a dotted square) are shown. Scale bar = 100 μm. **(J)** Scatter plot showing the expression of ST3GAL5 in lung normal and cancer tissues. Each point represents the H-score from a single tissue sample ranging from the total absence of ST3GAL5 (H-score 0) to very strong ST3GAL5 staining (H-score 300). H-scores are represented as mean ± SEM, normal tissues, n=48; cancer tissues, n=97, ****, P < 0.0001, based on an unpaired Student's t-test.

until first progression (Figure 7G) [46]. In addition, the mRNA expression levels of ST3GAL5 analyzed using the Oncomine database showed that ST3GAL5 is frequently expressed at low levels in various human cancer tissues, including lung cancer tissues, compared to respective normal adjacent tissues (Figure EV5E) [47-49]. This is consistent with the results obtained by the analysis of the Bhattacharjee Lung Cancer database: low levels of ST3GAL5 were detected in lung cancer compared to normal adjacent tissues (Figure 7H) [50, 51]. Moreover, we examined the ST3GAL5 protein levels in a tissue microarray with 150 lung cancer

tissues and adjacent phenotypically normal tissues derived from 50 patients by immunohistochemistry (IHC) staining with a ST3GAL5-specific antibody. ST3GAL5 was found highly expressed in adjacent normal tissues when compared to cancer tissues (Figure 7I). ST3GAL5 was barely present in the lung cancer tissues in different stages from Stage IA to IIIA with increased growth and metastatic abilities (Figure 7I, EV5F). The H-score quantification of ST3GAL5 confirmed that ST3GAL5 levels are low in adenocarcinoma lung tissues compared to normal adjacent tissues (Figure 7J, EV5G). These results suggest that ST3GAL5 expression inhibits cell migration and invasion and is associated with good prognosis in lung cancer.

Discussion

TGF-β-induced EMT is mediated via a decrease in *a*-series gangliosides

NMuMG and A549 cell lines are frequently used models for TGF-β-induced EMT. Profiling GSLs in both cell lines in the absence or upon several days of exposure to TGF-β showed the high similarities between GSLs in their basal epithelial state and those in a TGF-β-induced mesenchymal state. The *a*-series gangliosides, i.e., GM3, GM2, GM1a, and GD1a, were the most abundant GSLs in both cell lines. Low levels of certain *b*-series gangliosides, including GD3, were also detected both in NMuMG and A549 cells. Small amounts of (iso) globosides, i.e., Gb3 and Gb4, and (neo) lacto-series, i.e., Lc4, nLac4, and S(3)nLc4, were detected in A549 cells but not in NMuMG cells, while *o*-series gangliosides were only detected in NMuMG cells. The TGF-β-induced EMT in both cell lines was found to coincide with a striking decrease of all GSLs, especially the *a*-series gangliosides. Consistent with the TGF-β-induced downregulation of *a*-series gangliosides, TGF-β induces a decrease in ST3GAL5 mRNA and protein expression, the key enzyme of *a*-series ganglioside synthesis in NMuMG cells. Strikingly, genetic UGCG KO in NMuMG cells or the pharmacological inhibition of GSL synthesis in both NMuMG and A549 cells promoted TGF-β-induced EMT. It will be

interesting to explore if TGF-β-induced EMT in other patho-physiological contexts is also accompanied by a downregulation of *a*-series gangliosides.

A previous study reported on the expression and composition changes of gangliosides in human normal bladder HCV29 cells and mouse NMuMG cells during TGF-β-induced EMT [34]; Gg4 and GM2 were significantly reduced, and a slight but not significant decrease of GM1 and GM3 levels was reported in response to TGF-β stimulation. These findings are in accordance with our results in NMuMG cells [34].

UGCG and ST3GAL5 inhibit TGF-β signalling and EMT

The glycotransferase UGCG/ST3GAL5-mediated production of *a*-series gangliosides was identified as a critical negative modulator of TGF-β signalling. Comparing the transcriptional profiles of NMuMG cells that are wild-type or deficient in UGCG by GSEA for TGF-β gene response signatures revealed a negative correlation of Ugcg and TGF-β signalling in NMuMG cells. In agreement with this, q-PCR analysis revealed that the TGF-β-mediated promotion of TGF-β target genes, including *Smad7* and *Serpin1*, were more pronounced, and TGF-β-induced SMAD2 phosphorylation levels were enhanced in Ugcg knockout NMuMG cells. TGF-β/SMAD signalling is a main driver of EMT; thus, in line with this notion, GSEA using EMT gene signature sets in NMuMG cells revealed that Ugcg also negatively correlated with EMT. This was further validated by the TGF-β-induced downregulation of epithelial marker E-cadherin and the upregulation of mesenchymal marker N-cadherin at both mRNA and protein levels, whereas we used (initially) a genetic approach to inactivate Ugcg in NMuMG cells and a pharmacological approach to inhibit UGCG activity in A549 cells. Fully consistent with genetic inactivation, the inhibition of UGCG with eliglustat in A549 (and NMuMG) cells promoted TGF-β signalling and TGF-β-induced EMT.

Furthermore, we revealed the essential role of ST3GAL5-sythesised *a*-series gangliosides in inhibiting TGF-β signalling and EMT in A549 cells. ST3GAL5 knockdown, but not the depletion of B4GALNT1, mimicked the UGCG inactivation-induced effects on TGF-β signalling and EMT. Moreover, the exogenous addition of ST3GAL5-mediated *a*-series gangliosides, including GM3, GM2, and GM1a, antagonised TGF-β

signalling and the EMT of A549 cells. Thus, our findings narrow down the GSLs involved in TGF-β signalling and EMT to the specific branch of *a*-series gangliosides. In addition, these findings taken together with the TGF-β-induced decrease in *a*-series gangliosides, indicate that they participate in a self-enabling response for EMT promoted by TGF-β.

Of note, in human lens epithelial cells, the expression of GM3 promoted TGF-β signalling and TGF-β-induced EMT by a potential interaction with TβRs [52]. While we observed no significant difference on TGF-β signalling and EMT upon treatment with exogenous GD3, others reported that ST8SIA1, an enzyme involved in GD3 and GD2 biosynthesis, plays an important role in the initiation and maintenance of EMT [53]. Inhibition of this enzyme suppressed the invasion and motility of breast cancer cells as well as metastasis in mice [53]. Effects of specific gangliosides, such as GD3 and GM3, on EMT may vary in different cancer types.

Specific GSLs inhibit TGF-β signalling by favouring TβRI in lipid rafts

Mechanistically, we observed that UGCG-ST3GAL5-catalysed *a*-series gangliosides inhibited TGF-β signalling by favouring localisation of TβRI into lipid rafts. The latter is linked to an increase in TβRI ubiquitination and degradation. The inactivation of UGCG or ST3GAL5 depletion reduced the ubiquitination of TβRI, while the exogenous addition of the ST3GAL5-catalysed ganglioside GM3 promoted TβRI ubiquitination. The ubiquitylation of TβRI was previously shown to be intricately linked to the lysosomal/proteasomal degradation of receptors [9, 11]. Consistent with this notion, we found that the eliglustat-decreased and GM3-increased ubiquitination of TβRI reduced and elevated TβRI protein stability, respectively. Therefore, our results identify *a*-series gangliosides as an important determinant for TβRI membrane domain localisation and protein stability.

UGCG and ST3GAL5 inhibit cell migration and extravasation of lung A549 cells

In line with UGCG-ST3GAL5-mediated inhibitory action on TGF-β signalling and EMT, we found that UGCG inactivation or ST3GAL5

depletion strongly promoted TGF-β-induced A549 cell migration *in vitro* and extravasation *in vivo* using a zebrafish xenograft model. By demonstrating that the basal and TGF-β-induced migration/invasion by UGCG-ST3GAL5 inhibition was attenuated by the TGF-β kinase inhibitor SB505124, it can be concluded that these responses are dependent on TβRI signalling. Moreover, the addition of ST3GAL5-catalysed gangliosides, including GM3, GM2, and GM1a, antagonised the TGF-β-induced migration of A549 cells. Consistent with our results, chemoenzymatic synthesised ganglioside GM3 effectively inhibits the migration of melanoma B16–F10 cells [54]. Besides, the GM3 synthase overexpressed A2780 ovarian carcinoma cells were characterised by increased levels of caveolin-1 and a reduced *in vitro* cell motility [55]. Enhanced synthesis of GM3 also caused a decrease in the invasiveness in bladder cancer cells [56]. Our findings taken together with other reports demonstrate the inhibitory role of UGCG-ST3GAL5-synthesised *a*-series gangliosides in various cancer types.

ST3GAL5 expression correlates with good prognosis in lung cancer

Notably, data mining of RNA expression in publicly accessible databases of lung cancer mRNA profiles revealed that *ST3GAL5* expression correlates with favourable prognosis in lung cancer. Consistent with this notion, our immunohistochemical analysis of ST3GAL5 protein levels showed that ST3GAL5 is significantly less expressed in lung cancer tissues as compared to adjacent normal tissues. Our finding is in line with a study in which the expression of ST3GAL5 was analysed in bladder cancer patients by mining publicly available datasets; they reported that a low expression of ST3GAL5 is associated with muscle invasion, a high grade, and a poor prognosis in patients with bladder cancer [57]. Moreover, Kyoto Encyclopedia of Genes and Genomes (KEGG) pathway analysis for ST3GAL5 showed its association with TGF-β signalling [57]. In breast cancer, a high expression of ST8SIA1 was significantly correlated with poor overall survival, but not ST3GAL5 [58]. In addition, some gangliosides, i.e., GM2, GD2, and GD3, are highly expressed in various human tumours (melanomas, gliomas, neuroblastomas, and breast cancer) but are absent or weakly expressed in normal tissues [57, 59, 60]. All these

studies performed in different cancer subtypes suggest the pleiotropic nature of specific gangliosides and related enzymes in cancer progression.

In conclusion, we performed a quantitative glycomic analysis of GSLs in an in-depth manner and demonstrated that TGF-β-induced decrease in GSLs, in particular *a*-series gangliosides, in mouse normal epithelial NMuMG cells and human lung cancer A549 cells undergoing EMT. Since the inhibition of the *a*-series ganglioside synthesis mediated by ST3GAL5 promotes TGF-β signalling and TGF-β-induced EMT, cell migration, and invasion, the TGF-β-induced inhibition of these gangliosides enforces a TGF-β-induced EMT response. The *a*-series gangliosides that are enriched in lipid rafts stimulate the ubiquitination and degradation of TβRI. Moreover, we uncovered an association between highly expressed ST3GAL5 and a good prognosis of lung cancer patients. It will be interesting to explore the potential of ST3GAL5 as a prognostic biomarker and its potential as a molecular target for lung cancer therapy.

Materials and Methods

Cell culture

Mouse NMuMG epithelial cells, HEK 293T cells, human lung adenocarcinoma A549 cells, and A549-VIM-RFP cell lines were originally from American Type Culture Collection (ATCC) and cultured in Dulbecco's modified Eagle medium (DMEM, 11965092, Thermo) with 10% fetal bovine serum (FBS, S1860-500, BioWest) and 100 U/mL penicillin-streptomycin (15140148, Thermo). All cells were frequently tested for the absence of mycoplasma contamination, and all human cell lines were authenticated by short tandem repeat (STR) profiling.

Chemical and reagents

Ammonium bicarbonate (ABC), trifluoroacetic acid, cation exchange resin beads (AG50W-X8), potassium hydroxide, sodium borohydride, and cycloheximide (CHX) were obtained from Sigma-Aldrich (Steinheim, Germany). The UGCG inhibitor eliglustat was purchased from MedChemExpress (HY-14885A). The gangliosides GM1a (1545), GM2 (1542), GM3 (1503), GD3 (1504), and GT1b (1548) were purchased from

Matreya (Pennsylvania, USA). SB505124 was purchased from Tocris (3263). HPLC SupraGradient acetonitrile (ACN) was obtained from Biosolve (Valkenswaard, The Netherlands), and other reagents and solvents such as chloroform, methanol, 2-propanol, and glacial acetic acid were obtained from Merck (Darmstadt, Germany). The 50 mg tC18 reverse phase (RP) cartridges were from Waters (Breda, The Netherlands). Endoglycoceramidase I (EGCase I, recombinant clone derived from *Rhodococcus triatomea* and expressed in *Escherichia coli*) and 10x EGCase I buffer (500 mM HEPES, 1M NaCl, 20 mM DTT, and 0.1% Brij 35, pH 5.2) were purchased from New England BioLabs Inc. (Ipswich, MA).

Preparation of GSL-glycan alditols

The extraction of GSLs and the preparation of GSL-glycan alditols from cells were performed in triplicate as previously described [38] with slight modifications. Shortly, 2×10^6 cells were lysed by 200 µL of water. In prior to GSL extraction, 2.5 µL of 0.5 µM ganglioside GT1b in ethanol were added as a spiked internal standard to monitor sample preparation and normalise absolute quantification. Crude GSLs were extracted and dried under vacuum in an Eppendorf Concentrator 5301 (Eppendorf, Hamburg, Germany) at 30 °C. The extracted GSLs were dissolved in 100 µL of methanol followed by an addition of 100 µL water in prior to solid phase extraction (SPE) purification on tC18 RP cartridges. Eluate was collected and dried in an Eppendorf Concentrator. Next, a mixture of EGCase I (12 mU, 2 µL), EGCase I buffer (4 µL) and water (34 µL) (pH 5.2) was added to each sample and incubated for 36 h at 37 °C to release the glycan head group. The released glycans were further purified by tC18 RP cartridges. The flow-through and wash fractions were collected and dried in an Eppendorf Concentrator.

The reduction and desalting of GSL-glycans were carried out with slight modifications following the same procedure as described in previous studies [38, 61]. In brief, GSL-glycans were reduced to alditols in 30 µL of sodium borohydride (500 mM) in potassium hydroxide (50 mM) for 3 h at 50 °C. After desalting, the glycan alditols were collected by combining flow-through and eluate and dried in an Eppendorf Concentrator at 30 °C. A PGC SPE clean-up was performed to further

purify the samples. The purified glycan alditols were re-suspended in 200 µL of water prior to PGC nano-LC-ESI-MS/MS analysis.

Analysis of GSL-glycan alditols using PGC nano-LC-ESI-MS/MS

The analysis of glycan alditols was performed using PGC nano-LC-ESI-MS/MS following a method described previously [38, 61]. Measurements were performed on an Ultimate 3000 U high performance liquid chromatography (HPLC) system (Thermo) equipped with a home-packed PGC trap column (5 µm Hypercarb, 320 µm x 30 mm) and a home-packed PGC nano-column (3 µm Hypercarb 100 µm x 150 mm) coupled to an amaZon ETD speed ion trap (Bruker, Bremen, Germany). To analyse glycans, 2 µL of samples were injected. Separation was achieved with a linear gradient from 1% to 50% mobile phase B over 73 min at a 0.6 µL/min flow rate. The column was held at a constant temperature of 35 °C.

Ionisation was achieved using the nanoBooster source (Bruker) with a capillary voltage of 1000 V applied, a dry gas temperature of 280 °C at 3 L/min, and isopropanol-enriched nitrogen at 3 psi. MS spectra were acquired within an *m/z* range of 340–1850 in enhanced mode using negative ion mode. The smart parameter setting was set to *m/z* 900. MS/MS spectra were recorded using the three highest intensity peaks.

Glycan structures were assigned on the basis of the known MS/MS fragmentation patterns in negative-ion mode [37, 62, 63], elution order, and general glycobiological knowledge, with help of Glycoworkbench [64] and Glycomod [65] software. MS/MS mass lists with annotated structures were exported from the DataAnalysis software for upload to the Unicarb DR repository [39]. Relative quantification of individual glycans was performed by normalising the total peak area of all glycans within one sample to 100%. To estimate the glycan amount per cell, glycan intensity was normalised to the intensity of the internal standard GT1b. Afterwards, assuming the complete release of glycans and similar response factors between released glycan and GT1b standard, the number of glycans per cell was estimated. Structures are depicted according to the Consortium of Functional Glycomics (CFG). The blue square is *N*-acetylglucosamine; the yellow square is *N*-acetylgalactosamine; the blue circle is glucose; the yellow circle is galactose; the red triangle is fucose; the purple diamond is

N-acetylneuraminic acid; the grey diamond is *N*-glycolylneuraminic acid. In the figures containing glycan structures, black arrows indicate gangliosides, green arrows indicate globosides, and blue arrows indicate neolacto series GSL.

Quantitative real-time-polymerase chain reaction (qRT-PCR)

Total RNA extraction was prepared using the NucleoSpin RNA II kit (740955, BIOKE´). The concentration of RNA was determined by NanoDrop™ 2000/2000c (Thermo), and a total of 1 μg of RNA was retro-transcribed using the RevertAid First Strand cDNA Synthesis Kit (K1621, Thermo). Real-time reverse transcription-PCR was conducted with SYBR Green (GoTaq DNA Polymerase, PROMEGA) using the CFX Connect Detection System (1855201, Bio-Rad). The DNA primer sequences that were used to detect the expression of specific genes are listed in Table S2. All target gene expression levels were normalised to glyceraldehyde 3-phosphate dehydrogenase (*GAPDH*). Results are shown as technical triplicates and representative of three independent biological experiments.

UGCG knockout by CRISPR/Cas9

The mouse sgRNAs of UGCG (forward: 5'-CACCTCGTGCTCTTCGTG GTGCTG-3'; reverse: 5'-AAACCAGCACCACGAAGAGCACGA-3') were provided by Dr. Robbert M Spaapen (Sanquin Research, Amsterdam) and were cloned into the lentiviral vectors lentiCRISPR_v2 (Addgene) [66]. The design and cloning of sgRNA were performed according to the general protocols obtained from the Feng Zhang lab [67, 68]. The pLV-Cas9-blasticidin plasmid (CAS9BST, Sigma) was used as a negative control.

For lentivirus production, the cloned 1 lentiCRISPR_v2 with UGCG sgRNA inserts or the pLV-Cas9 plasmid [69] was co-transfected into HEK293T cells with three packaging plasmids: pVSVg, psPAX2, and pAdv. The lentivirus was harvested at 48 h post-transfection and filtered through a 0.45 μm polyethersulfone (PES) filter. Viruses were either directly used for infection or quickly stored at -80 °C to avoid loss of titre.

To generate the stable NMuMG cells with UGCG knockout, we firstly prepared a 1:1 dilution of the pLV-Cas9 lentivirus in completed DMEM with 5 ng/mL polybrene (Sigma). Afterwards, NMuMG cells were

infected with the lentiviral dilution at a low cell density (30%), and cells were selected with 4 μg/mL blasticidin (R21001, Invitrogen) for one week after 24 h of infection to generate NMuMG cells with Cas9 expression. Once the Cas9 expression was validated, the NMuMG cells were further infected with UGCG sgRNA lentivirus and selected by DMEM medium with 1 μg/mL puromycin for one week. Thereafter, two single cell colonies were picked up under microscope, and cells were then cultured and expanded.

UGCG activity assay

Cas9 and UGCG KO clones were pelleted and resuspended in Buffer Q (10mM Tris 7.0, 10mM NaCl and 0.5mM EDTA). Cells were lysed by passing them 10 times through a 26G needle. Post-nuclear supernatant was collected by centrifuging for 5 min at 900x *g*. A post-nuclear supernatant equivalent to 100,000 cells in 50 μL was combined with Buffer Q supplemented with 3.2 mM UDP-Glucose (Sigma cat# 94335) and 1 mM BSA-coupled BODIPY-C5-Ceramide (ThermoFisher cat# B22650). Reactions were incubated for 1 h at 37 ºC with constant shaking. Next, samples were supplemented with 100 μL of 2% NaCl and subjected to standard Bligh-Dyer lipid extractions (PMID: 13671378). Lipids were dried and resuspended in chloroform/methanol (2:1, v/v) and spotted on a thin-layer chromatography plate. Plates were developed in chloroform/acetone/acetic acid/methanol/water (50:20:10:10:5, v/v/v/v/v). Dried plates were imaged using a GE Typhoon FLA 9500 imager using a 488 nm laser and 530/20 (BPB1) band-pass filters.

Small interfering RNA (siRNA) transfections

A549-VIM-RFP cells were transfected with non-targeting (4390843, Dharmacon), ST3GAL5 (L-011546-00-0005, Dharmacon), or B4GALNT1 (L-011279-00-0005, Dharmacon) siRNAs mixed with transfection reagent DharmaFECT1 #1 (T-2001, Dharmacon). The mixture was incubated in a serum-free medium for 20 min at room temperature and then added to cells. After three days of transfection, the target gene knockdown efficiencies of the cells were analysed using qRT-PCR.

Dynamic detection of RFP-vimentin expression assay

A549-VIM-RFP cells (in which the red fluorescent protein coding region is closed with the VIMENTIN locus) were used as a model system to indicate EMT by analysing the changes of RFP-tagged vimentin expression. The near confluent cells with the indicated treatment were cultured in a 96-well plate in the IncuCyte live cell imaging system. The RFP signals were captured every 2 or 4 h over a period of 48–72 h using a 10 × objective. The RFP-vimentin density was then analysed by the IncuCyte software and normalised by the RFP signals at 0 h for each group. All the experiments were performed with biological triplicates, and representative results are shown.

CAGA-GFP Transcriptional Response Assay

A549-VIM-RFP cells were infected by pLV-$CAGA_{12}$-green fluorescent protein (GFP) lentivirus and selected with 1 μg/mL puromycin for one week to obtain the cells stably expressing a SMAD3/4-dependent $CAGA_{12}$-transcriptional GFP reporter. Thereafter, the A549-VIM-RFP cells with CAGA-GFP were seeded in a 96-well plate and incubated in the IncuCyte live cell imaging system (Essen BioScience). The $CAGA_{12}$-mediated transcriptional activity was measured every 1 h over a 25 h-period using a 10× objective and normalised by the GFP signals at 1 h. All the experiments were performed with biological triplicates, and representative results are shown.

Ubiquitination, immunoprecipitation, and immunoblotting

HEK293T cells were transfected with Myc-tagged constitutively active TβRI (Myc-caTβRI) and HA-ubiquitin (HA-Ub) for 48 h and treated with 5 μM proteasome inhibitor MG132 (474787, Sigma) for 6 h before harvesting. Cells were then harvested and washed twice in cold phosphate buffered saline (PBS) with 10 mM N-ethlmaleimide (NEM) and lysed in 1% sodium dodecyl sulphate (SDS)-RIPA buffer (25 mM Tris-HCl, pH7.4, 150 mM NaCl, 1% NP40, 0.5% sodium deoxycholate, and 1% SDS) supplemented with protease inhibitors (11836153001, Roche) and 10 mM NEM for 10 min on ice. The lysates were centrifuged at 11×10^3g for 10 min at 4 °C, and the protein concentrations were then measured using the DC protein assay (Pierce). To prevent the detection of any

ubiquitination of co-immunoprecipitating proteins, the lysates were boiled for 5 min, diluted to 0.1% SDS in an RIPA buffer, and followed up with immunoprecipitation analysis. For the immunoprecipitation assay, equal amounts of protein were incubated with an anti-Myc antibody overnight and the protein G-Sepharose (GE Healthcare Bio-Sciences AB) for 2 h at 4 °C. Thereafter, beads were washed five times with a TNE buffer at 4 °C and boiled with a sample buffer for 5 min. The immunoprecipitated proteins were then separated by SDS-PAGE. For immunoblotting, equal amounts of proteins were loaded on a gel, and proteins were separated by SDS polyacrylamide gel electrophoresis (PAGE). Afterwards, proteins were transferred onto a 45 μm polyvinylidene difluoride (PVDF) membrane (IPVH00010, Merck Millipore) and analysed using specific primary and secondary antibodies. Signals were visualised with chemiluminescence. All experiments were performed with biological triplicates, and representative results are shown.

The antibodies used for immunoprecipitation (IP) and immunoblotting (IB) are as follows: phosphor-SMAD2 1:1000 (IB: 3108, cell signalling), total-SMAD2 1:1000 (IB: 3103S, cell signalling), GAPDH 1:1000 (IB: MAB374, Millipore), Tubulin 1:1000 (IB: 2148, cell signalling), E-Cadherin 1:1000 (IB: 610181, BD Biosciences), N-cadherin 1:1000 (IB: 610920, BD Biosciences), vimentin 1:1000 (IB: 5741, cell signalling), SNAIL 1:1000 (IB: 3879, cell signalling), vinculin (IB: V9131, Sigma), Flotillin-1 1:1000 (IB: sc-25506, Santa Cruz), β1-integrin 1:1000 (IB: ab183666, Abcam), EEA1 1:1000 (IB: 610457, BD Biosciences), ST3GAL5 1:1000 (IB: NBP2-20492, Novus Biologicals), c-Myc 1:200 (IP: sc-40, Santa Cruz), HA 1:1000 (IB: 1583816, Roche), and TβRI 1:1000 (IB: sc-398, Santa Cruz).

Separation of lipid raft and non-lipid raft microdomains of plasma membranes

Sucrose density gradient analysis was performed as described previously [70]. In brief, 1×10^8 cells were digested by trypsin and washed with ice-cold PBS twice. The cells were then pelleted by centrifugation at 290× *g* for 4 min, and the supernatant was discarded. Thereafter, 1.4 mL of membrane raft isolation TNVE buffer (1% Triton X-100, 10 mM Tris–HCl, pH 7.5, 150 mM NaCl, 5 mM EDTA, 1 mM Na_3VO_4) containing a

freshly added protease inhibitor cocktail was added to resuspend the cell pellet. The cell lysate was then transferred to a pre-cooled tightfitting Dounce homogeniser and kept on ice for 60 min. Thereafter, cell homogenisation was carried out with 10 strokes. The homogenised cells were transferred into a 15 mL plastic tube and centrifuged at 200× *g* for 8 min at 4 °C. One milliliter of supernatant was mixed with 1 mL of 85% (w/v) sucrose in a TNEV buffer and transferred to the bottom of a 14 mL Beckman centrifuge tube (344060). Six milliliters of 35% (w/v) sucrose in the TNEV buffer were carefully added on top of the diluted cell lysate using a 1 mL pipette and followed up with 3.5 mL of 5% (w/v) sucrose in the TNEV buffer on its top. Once the centrifuge tubes are loaded, each tube was placed into the compatible ultracentrifuge rotor (SW 40 Ti, Beckman) and balanced with a TNEV buffer. The loaded tubes were centrifuged at 257,000× *g* for 18 h at 4 °C with the brake off to ensure that deceleration did not disrupt the density gradient. After centrifugation, centrifuge tubes were carefully taken out from the rotor. One milliliter of each fraction was collected from the top of the gradient until the end of the tube. The individual fractions were subjected to SDS-PAGE and analysed by immunoblotting analysis. All experiments were repeated three times in biologically independent experiments, and representative results are shown.

IncuCyte Migration Assay

Cells were seeded in the IncuCyte 96-well Essen ImageLock plate (4379, Essen BioScience) and scratched using the IncuCyte WoundMaker (Essen BioScience). The scratched cells were washed with phosphate buffered saline (PBS) and then cultured with DMEM medium with 10% serum in the IncuCyte live cell imaging system. Images were acquired every 2 or 4 h over a 36–68 h period using a 10× objective. Relative wound density was analysed by the IncuCyte cell migration software for each well. All experiments were performed with biological triplicates, and representative results are shown.

Zebrafish extravasation assay

The A549 cells were infected with pLV-mCherry lentivirus and subjected to FACS sorting to obtain a pool of cells that highly expresses mCherry.

Thereafter, the mCherry-labelled A549 cells were applied to the zebrafish experiment. We used the transgenic green fluorescent zebrafish *Tg fli*: enhanced green fluorescent protein (EGFP) strain for our xenograft cancer model. The experiments were carried out according to the standard guidelines approved by the local Institutional Committee for Animal Welfare of the Leiden University. The zebrafish extravasation assay was performed as previous described [71]. Briefly, A549-mCherry cells were transfected with the indicated siRNAs for three days or pre-treated with indicated inhibitors for six days. Thereafter, approximately 400 cells were injected into the ducts of Cuvier of zebrafish embryos at 48 h post-fertilisation. Four days after injection, the fish were fixed with 4% paraformaldehyde (PFA, 28908, Thermo Fisher Scientific) and imaged by inverted SP5 confocal microscopy (Leica Microsystems). The invasive cell clusters (more than five cells were defined as a cluster) between the vessels in the caudal hematopoietic tissue region were counted. The experiments were repeated twice in biologically independent experiments, and at least 25 injected embryos were included for quantification.

Immunofluorescence staining

Cells were seeded onto sterile 18 mm long square glass coverslips (631-1331, Menzel Gläser) and cultured with complete DMEM. After the indicated treatment, the cells were fixed with 4% PFA for 30 min and permeabilised with 0.1% Triton X-100 for 10 min at room temperature. Afterwards, 5% bovine serum albumin (BSA) (A2058, Sigma-Aldrich) in 0.1% PBS-Tween was used for 1 h to block the cells. The 1:1000 diluted primary antibody of E-cadherin (610181, BD Biosciences) in PBS was incubated with cells for 1 h. Thereafter, the cells were washed with PBS three times and incubated with a 1:500 diluted Alexa Fluor 555 secondary antibody (A-21422, Thermo) or 1:1000 diluted Alexa Fluor 488 Phalloidin (A12379, Thermo) for 1 h. The cells were then washed with PBS three times and mounted with a VECTASHIELD antifade mounting medium with 4',6-diamidino-2-phenylindole (DAPI, H-1200; Vector Laboratories). SP8 confocal microscopy was used to capture images (Leica Microsystems). All experiments were performed in biological triplicates, and representative results are shown.

Flow cytometry

The cells with UGCG knockout or those treated with eliglustat were harvested and counted using a cell counter. Thereafter, 2×10^5 cells were incubated with 50 µL of the diluted FITC-conjugated Cholera Toxin B subunit (CTB, C1655, Sigma) in PBS with the final concentration of 20 µg/mL for 30 min at 4 °C. Afterwards, 150 µL of PBS/bovine serum albumin (BSA) was added to the cells, and samples were further analysed on BD flow cytometers (Canto, Fortessa, LSR II or ARIA II). FACS data were analysed by FlowJo (Tree Star, Inc).

RNA sequencing

Library preparation and sequencing were performed by the Beijing Genomics Institute (BGI) in China. Total RNA was extracted using the NucleoSpin RNA II kit (740955, BIOKE´) following the manufacturer's instructions. Briefly, purified mRNA was poly-A selected using oligo dT beads and fragmented with the fragmentation enzyme. The first and second strand synthesis was then performed using random N6-primed reverse transcription. The synthesised cDNA was subjected to end-repair and was then 3' adenylated. After amplification by PCR and cyclisation by splint oligo and DNA ligase, RNA sequence reads were mapped on the DNBSEQ platform. RNA-Seq files were processed using the open-source BIOWDL RNA-seq pipeline v5.0.0 (https://zenodo.org/record/5109461 #.Ya2yLFPMJhE) developed at the LUMC. This pipeline performs FASTQ pre-processing (including quality control, quality trimming, and adapter clipping), RNA-Seq alignment, read quantification, and optional transcript assembly. FastQC was used for checking raw read QC. Adapter clipping was performed using Cutadapt (v2.10) with default settings. RNA-Seq reads' alignment was performed using STAR (v2.7.5a) on the GRCm39 mouse reference genome. The gene read quantification was performed using HTSeq-count (v0.12.4) with setting "–stranded=no". The gene annotation used for quantification was Ensembl version 104. Using the gene read count matrix, counts per million mapped (CPM) was calculated per sample on all annotated genes. In total, 11,218 genes with a higher CPM than 1 in at least 25% of all samples are kept for downstream analysis. The RNA samples used for sequencing were prepared with three biological triplicates.

Dataset acquisition and processing

We used the Oncomine (www.oncomine.org) [72, 73] public bioinformatics database to obtain a summary of ST3GAL5 expression in 20 types of cancer vs. healthy tissues. The threshold was designed with the following parameters: a fold change of 1.5, a p-value of 0.05, and a gene ranking of 10%. Box plots of the *ST3GAL5* gene expression levels in the lung cancer tissues and normal tissues in the Bhattacharjee Lung database were analysed from the Oncomine bioinformatics database, and the P value for statistical significance was set up as 0.05 [51]. The Kaplan–Meier curve of the first progression survival of lung cancer patients linked with ST3GAL5 mRNA expression was analysed from a public bioinformatics database Kaplan–Meier plotter (kmplot.com/analysis). The first progression (FP) survival of 982 patients was collected with a mean follow-up of 180 months. When the gene ST3GAL5 was uploaded to the database, samples were divided into two cohorts according to the median expression of ST3GAL5 (high vs. low expression) to obtain the Kaplan–Meier survival plots. The log-rank P-value and the hazard ratio (HR) with 95% confidence intervals were calculated and displayed on the web page.

For GSEA, we used the GSEA tool. We uploaded all genes with normalised count information from RNA sequencing analysis and ran it under default conditions with the gene symbol annotation [74, 75]. The mouse COULOUARN_TEMPORAL_TGFB1_SIGNATURE_ UP gene set [76] and the human TGFB_UP.V1_UP gene set [77] were used as TGF-β gene signatures. The mouse GOTZMANN_EPITHELIAL_TO_ MESENCHYMAL_TRANSITION_UP gene set [78] and the human SARRIO_EPITHELIAL_MESENCHYMAL_ TRANSITION_UP gene set [79] were used as EMT gene signatures.

Immunohistochemical (IHC) staining and evaluation

The formalin-fixed paraffin-embedded microarray of lung cancer tissues including matched lung cancer and adjacent normal tissues was purchased from Biomax (LC1504), and details of every tissue are listed in Figure S8. The tissue microarray was baked overnight at 37 °C and then for 2 h at 60 °C until the paraffin melted. The slide was then placed in a xylene bath

for 5 min three times. Thereafter, the slide was rehydrated in fresh absolute ethanol for 5 min twice and rinsed in methanol with 0.5% hydrogen peroxide for 20 min to block the activity of endogenous peroxidases. Subsequently, the slide was transferred once through 96%, 70%, and 50% ethanol, respectively, for 3 min each and washed with PBS containing 0.1% Tween-20. The washed slide was boiled in an antigen unmasking buffer (1.5M Tris, pH 8.0, 0.5M EDTA, 10% Tween-20) for 30 min using a pressure cooker. The tissue microarray was then washed with PBS/Tween three times and incubated with a 1:100 diluted primary ST3GAL5 antibody in PBS containing 1% BSA overnight at 4 °C. Thereafter, the 1:200 diluted biotinylated secondary antibody (E3053, DAKO) in PBS/BSA was added onto the tissue array for 30 min at room temperature after washing the slide with PBS/Tween three times. The slide was then incubated with Vectastain complex (PK-6100, Vector Laboratories) for 30 min at room temperature and washed with PBS/Tween three times and with 0.5M Tris-HCl, pH 7.4 once. A 0.05% 3,3'-diaminobenzidine (DAB) substrate solution with freshly added 0.015% H_2O_2 in 0.5M Tris-HCl was applied to the sections on the slide for less than 5 min, until the desired colour intensity was reached. Haematoxylin (517-28-2, KLINIPATH) was used to counterstain nuclei for 10 s. The slide was then rinsed in running tap water for 10 min. Subsequently, the tissue slide was dehydrated through 50%, 70%, 96%, and 100% ethanol, respectively, for 5 min each and washed with xylene twice, followed by further mounting with Entellan (107961, Merck Millipore). The colour of the antibody staining in the tissue sections was imaged by a 3DHistech Pannoramic slide scanner.

The quantification of IHC staining was expressed as H scores, which were calculated as previous described [80]. H scores are between 0 and 300 and calculated by the following formula: 3 × the percentage of cells with strong staining + 2 × the percentage of cells with moderate staining + 1 × the percentage of cells with weak staining. The analysis of tissue sections was unbiased.

Statistical analysis

Statistical analyses were performed with a Student's unpaired t-test using Prism 8 software (GraphPad La Jolla, CA) or as indicated in the legends.

P-value is indicated by asterisks in the figures: *$P \leqslant 0.05$, **$P < 0.01$, ***$P < 0.001$, ****$P < 0.0001$. $P \leqslant 0.05$ was considered statistically significant.

Acknowledgments

We are grateful to Robbert M Spaapen for providing the UGCG KO plasmids and reagents and to Marlieke Jongsma for the anti-EEA1 antibody. We thank Maarten A. H. van Dinther and Midory Thorikay for technical assistance, Sijia Liu and Jiang Ren for the zebrafish platform development, and all members of our laboratories for valuable discussion. We thank Babak Mousavi Gourabi and Boudewijn PT Kruithof for help with IHC staining. We acknowledge the support of the Chinese Scholarship Council (CSC) to Jing Zhang and Jin Ma, the Dutch Cancer Society (KWF) grant [BUIT 2015-7526], the Cancer Genomics Centre in the Netherlands (CGC. NL), and the ZonMW grant (09120012010061) to Peter ten Dijke.

Data availability section

The raw mass spectrometric data files that support the findings of this study are available in GlycoPOST in mzXML format, with the identifier GPST000243, accessible via the following link: https://glycopost.glycosmos.org/entry/GPST000243. MS/MS spectra of glycan structures with peak lists and fragmentation annotations are available via an online repository Unicarb DR [39] (https://unica rb-dr.biomedicin e.gu.se/).

Sequencing data has been deposited to a publically available GEO dataset with an accession number of GSE192691 (https://www.ncbi.nlm. nih.gov/geo/query/ acc.cgi?acc=GSE192691).

Expanded View Figures

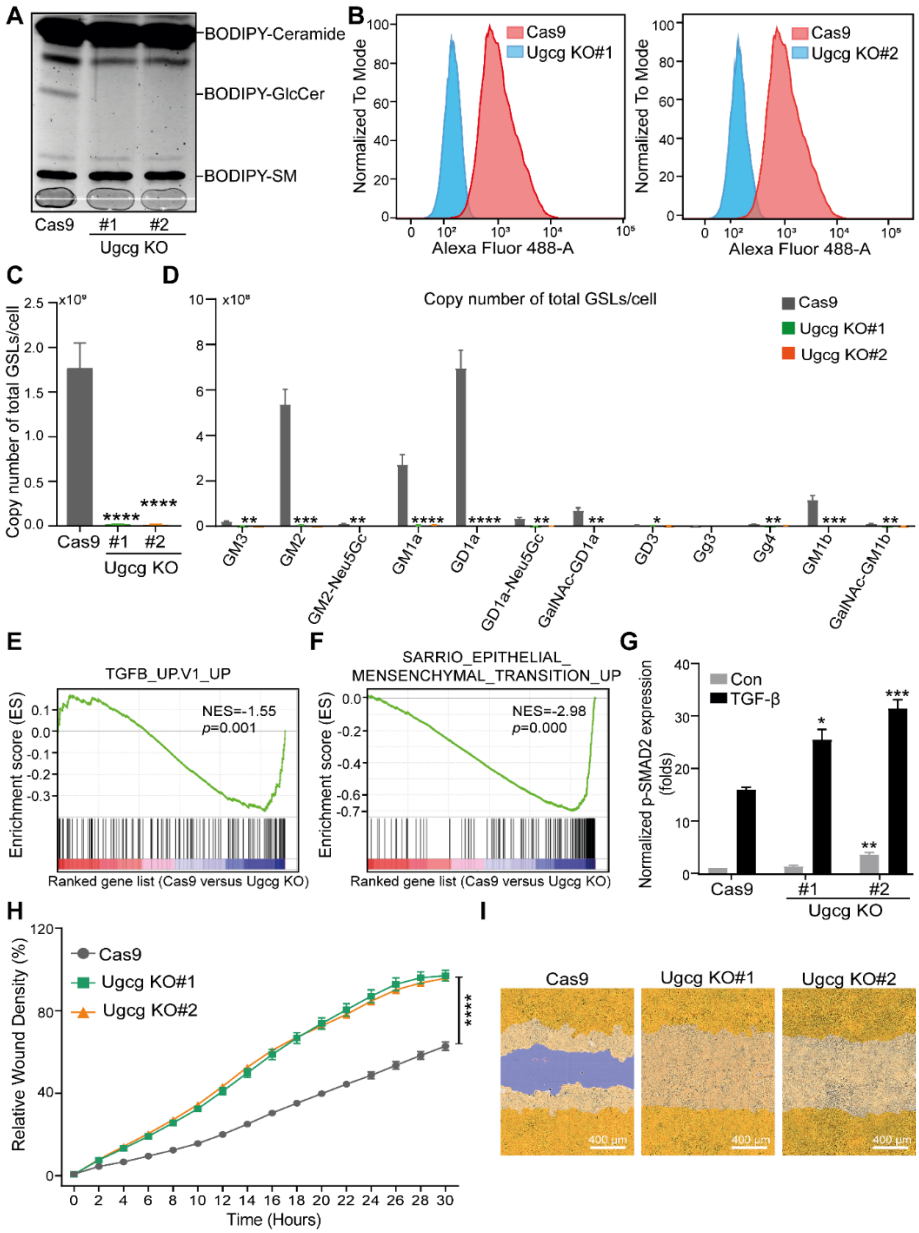

Figure EV1, related to Figure 2. Knockout of Ugcg promotes TGF-β signalling, EMT and migration of NMuMG cells. (A) Analysis of BODIPY-conjugated ceramide, glucosylceramide (GlcCer), and sphingomyelin (SM) in two independent Ugcg KO NMuMG cell lines and the NMuMG control cell line using thin layer chromatography (TLC) analysis. **(B)** Detection of GM1 ganglioside by flow cytometry using Alexa-488

fluorophore-conjugated cholera toxin subunit B (CTB) in two Ugcg knockout (KO#1 and KO#2) NMuMG cell lines infected with one guide RNA and a Cas9 expression vector or a Cas9 expression vector (control). **(C)** Average copy numbers of the total GSL-glycans per cell in NMuMG cells with Ugcg KO. **(D)** Average copy numbers of individual GSL-glycan per cell in NMuMG cells with Ugcg KO. **(E)** Human TGF-β gene response signature is enriched in NMuMG cells with Cas9 versus Ugcg KO shown by gene-set enrichment analysis (GSEA). Normalized Enrichment Score (NES) = -1.55, p = 0.001. **(F)** GSEA of human EMT gene signature enriched in NMuMG cells with Cas9 versus Ugcg KO. NES = -2.98, p = 0.000. **(G)** Quantification of p-SMAD2 expression in NMuMG cells including the Cas9 group and the Ugcg KO groups with or without TGF-β (2.5 ng/mL) treatment for 1 h. Tubulin: loading control. **(H)** Time course for scratch assay results in NMuMG cells without or with Ugcg deficiency analyzed by IncuCyte. **(I)** Representative images of a scratch wound at the end time point (30 h) in the control group and two Ugcg KO groups in NMuMG cells. The region of the original scratch is indicated in purple, and the area of the cell is colored in yellow. Scale bar = 400 μm. Data information: In (C, D), data are expressed as mean ± SD, n=3. In (G, H), data are expressed as mean ± SEM, n=3. *, $P \leqslant 0.05$, **, $P < 0.01$, ***, $P < 0.001$, ****, $P < 0.0001$, based on an unpaired Student's t-test.

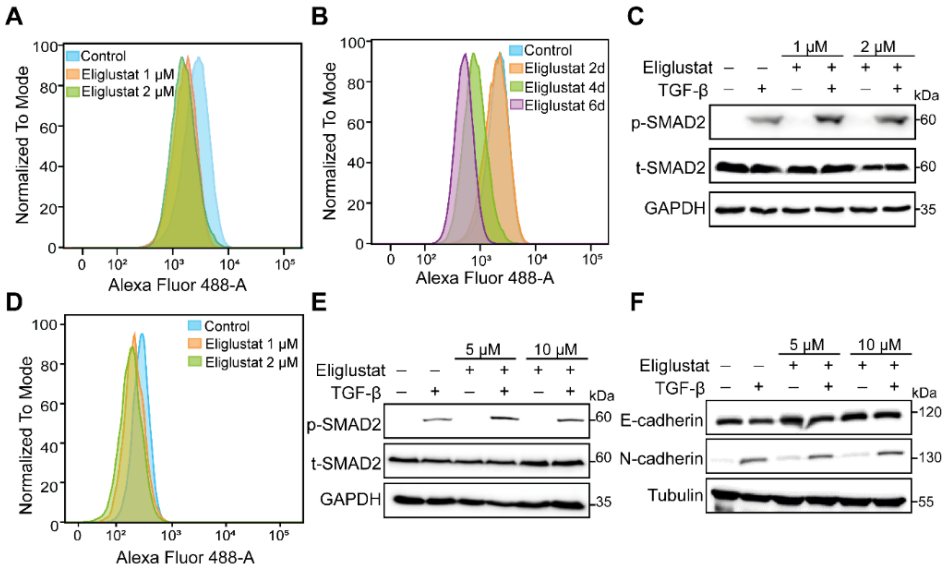

Figure EV2, related to Figure 3. UGCG inhibitor/Eliglustat promotes TGF-β signalling and TGF-β-induced EMT. (A) GM1 ganglioside detection in A549-VIM-RFP cells upon eliglustat treatment (1 μM or 2 μM) for 6 days, as analyzed by flow cytometry using Alexa-488 fluorophore-conjugated cholera toxin subunit B (CTB). **(B)** Analysis of GM1 ganglioside expression in A549-VIM-RFP cells upon eliglustat (2 μM) treatment for 2, 4, and 6 days, as analyzed by flow cytometry using Alexa-488 fluorophore-conjugated CTB. **(C)** Expression levels of p-SMAD2 and t-SMAD2 in A549-VIM-RFP cells pretreated with eliglustat (1 μM or 2 μM) for 4 days and combined with TGF-β (2.5 ng/mL) or vehicle control for another 2 days, as shown by immunoblot analysis. GAPDH: loading control. **(D)** Detection of GM1 ganglioside expression in NMuMG cells upon treatment with eliglustat (1 μM or 2 μM) for 4 days, as analyzed by flow cytometry using Alexa-488 fluorophore-conjugated CTB. **(E)** Immunoblot analysis of p-SMAD2 and total SMAD2 (t-SMAD2) expression in NMuMG cells that were treated with eliglustat (5 μM or 10 μM) for 4 days or vehicle control and/or TGF-β (2.5 ng/mL) for 1 h. GAPDH: loading control. **(F)** Western blot analysis of expression of epithelial marker E-cadherin and mesenchymal marker N-cadherin in NMuMG cells (pre)treated with eliglustat (5 μM or 10 μM) for 4 days and vehicle control and/or TGF-β (2.5 ng/mL) for 2 days. Tubulin: loading control.

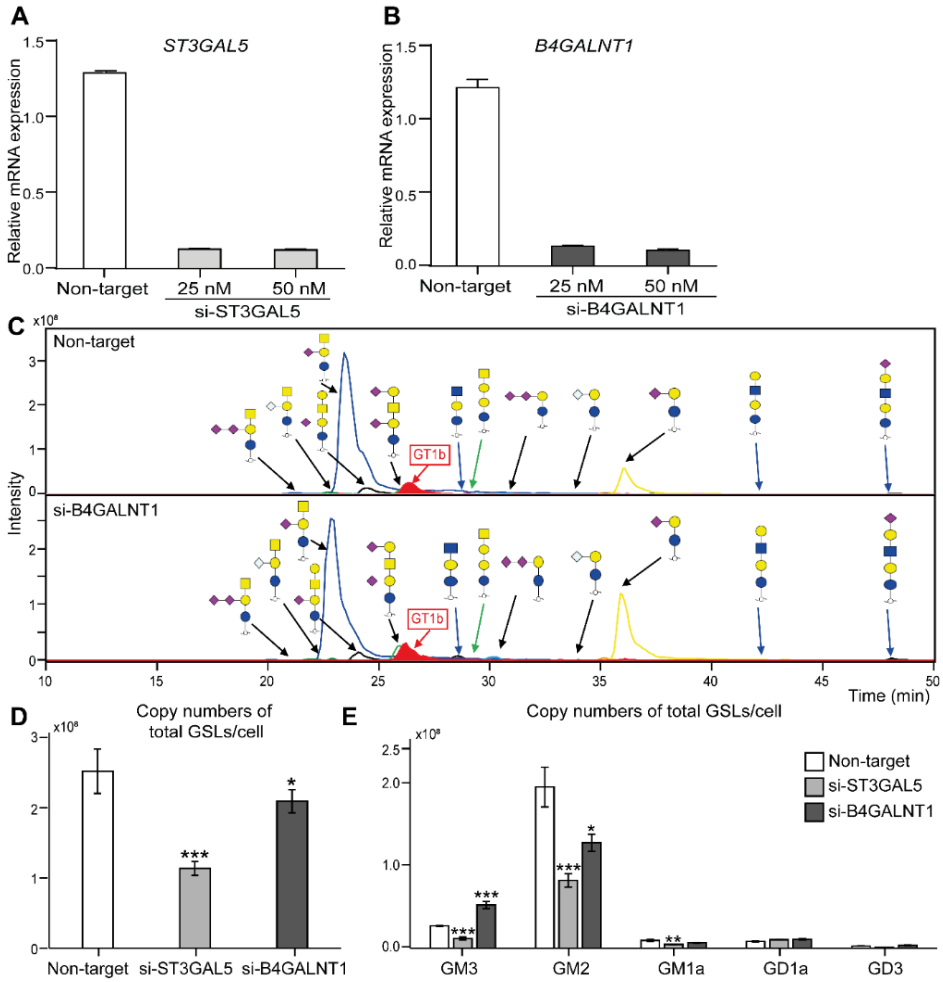

Figure EV3, related to Figure 5. Changes of GSLs in A549-VIM-RFP cells with ST3GAL5 and B4GALNT1 siRNAs. (A) qRT-PCR analysis of *ST3GAL5* in A549-VIM-RFP cells transfected with non-targeting siRNA and different concentrations of ST3GAL5 selective siRNA (at 25 nM and 50 nM). **(B)** qRT-PCR analysis of *B4GALNT1* expression in A549-VIM-RFP cells with non-targeting controls and si-B4GALNT1 (at 25 nM and 50 nM). **(C)** Combined extracted ion chromatograms (EIC) of GSL-glycans released from A549-VIM-RFP cells transfected with non-targeting, ST3GAL5, or B4GALNT1 siRNAs. GT1b was used as an internal standard for normalization. **(D)** Average copy numbers of the total GSL-glycans per cell in A549-VIM-RFP cells with non-targeting, ST3GAL5, or B4GALNT1 siRNAs. **(E)** Average copy numbers of the 5 major GSL-glycans per cell in A549-VIM-RFP cells with non-targeting, si-ST3GAL5, or si-B4GALNT1 siRNAs. Data information: In (B, C), data are expressed as mean ± SD, n=3. *, $P \leqslant 0.05$, **, $P < 0.01$, ***, $P < 0.001$, based on an unpaired Student's t-test. In (D, E), data are expressed as mean ± SEM.

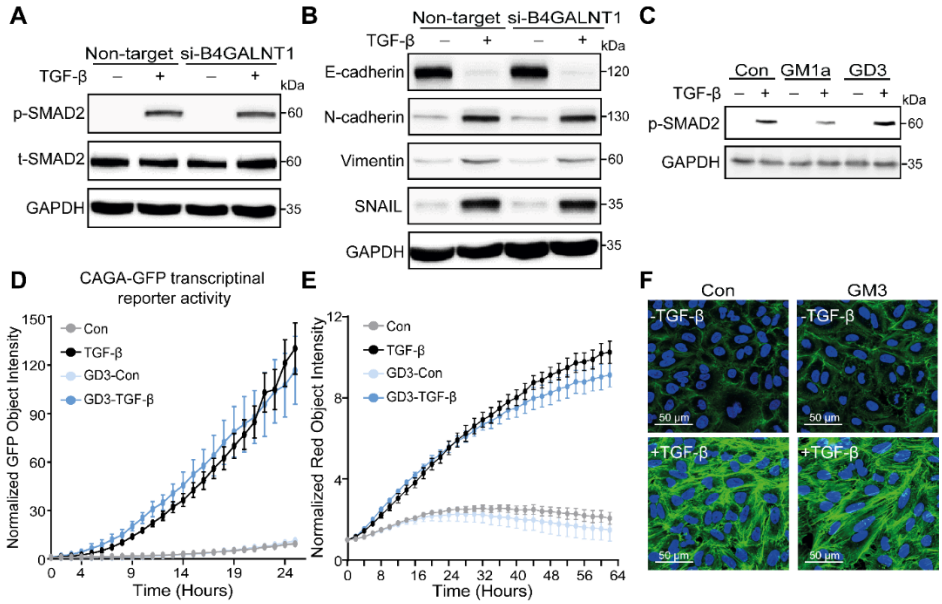

Figure EV4, related to Figure 5. Knockdown of B4GALNT1 or addition of GD3 has no effect on TGF-β signalling or EMT. (A) Immunoblot analysis of p-SMAD2 and t-SMAD2 expression levels in A549-VIM-RFP cells transfected with 25 nM non-targeting siRNA or B4GALNT1 siRNA with vehicle control or TGF-β treatment for 1 h. GAPDH: loading control. **(B)** Immunoblot analysis of expression of epithelial marker E-cadherin and mesenchymal markers N-cadherin, vimentin, and SNAIL in non-targeting groups or si-B4GALNT1 groups of A549-VIM-RFP cells treated with vehicle control or TGF-β for 2 days. GAPDH: loading control. **(C)** A549-VIM-RFP cells were pre-treated with 50 μg/mL GM1a or GD3 for 24 h and then treated with vehicle control or TGF-β for 1 h. Expression levels of p-SMAD2 were analyzed by western blot. GAPDH: loading control. **(D)** SMAD3/SMAD4-dependent $(CAGA)_{12}$-mediated transcriptional GFP reporter expression levels were measured in A549-VIM-RFP cells with CAGA-GFP lentivirus pre-treated with 50 μg/mL GD3 for 24 h and then combined with vehicle control or TGF-β for the indicated time points. The GFP object intensity was normalized by the green intensity at 0 h and presented as the mean ± SEM, n=3; no statistically significant difference, based on an unpaired Student's t-test. **(E)** Time course for the expression of RFP-conjugated vimentin measured by IncuCyte of A549-VIM-RFP pre-treated with 50 μg/mL GD3 for 24 h and thereafter challenged with vehicle control or TGF-β for the indicated times. Red object intensity was normalized by the red intensity at 0 h and presented as the mean ± SEM, n=3; no statistically significant difference, based on an unpaired Student's t-test. **(F)** Alexa-488 phalloidin staining for F-actin (green) in A549-VIM-RFP cells pre-treated with 50 μg/mL GD3 for 24 h and combined with vehicle control or TGF-β for another 48 h. Nuclei were counterstained with DAPI (blue). Images were captured with confocal microscopy. Scale bar = 50 μm. Data information: TGF-β was applied at a final concentration of 2.5 ng/mL.

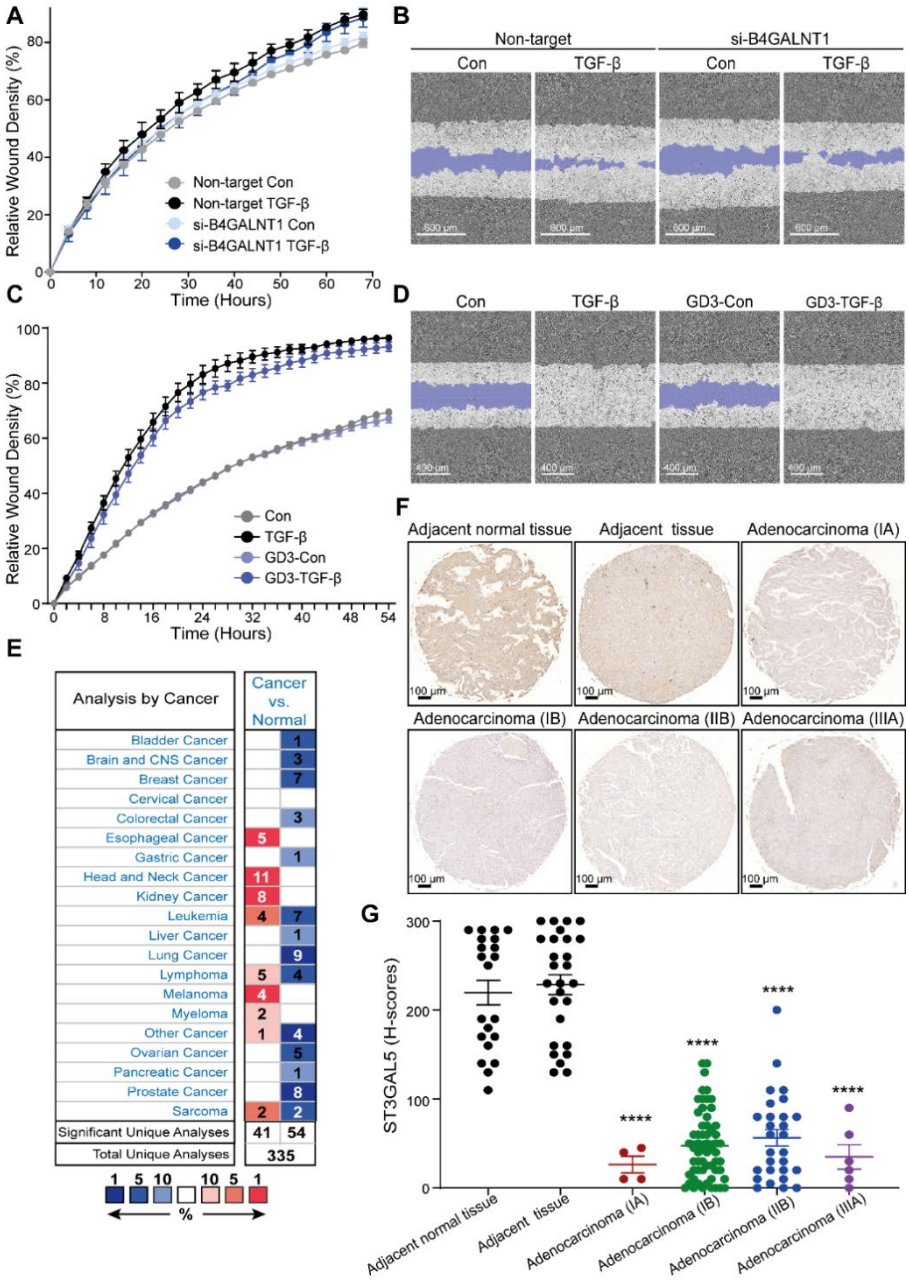

Figure EV5, related to Figure 7. Knockdown of B4GALNT1 or addition of GD3 has no effect on cell migration or ST3GAL5 expression in lung cancer tissues. (A) Real-time scratch assay results of non-target and si-B4GALNT1 A549-VIM-RFP cells with vehicle control or TGF-β (2.5 ng/mL) treatment for the indicated times. **(B)** Representative images of a scratch wound at the end time point (68 h) in the non-target

group and the B4GALNT1 knockdown group treated with vehicle control or TGF-β (2.5 ng/mL) in A549-VIM-RFP cells. The region of the original scratch is indicated in purple. Scale bar = 600 μm. **(C)** Time course for scratch assay results in A549-VIM-RFP cells pre-treated with 50 μg/mL GD3 for 24 h and then combined with vehicle control or TGF-β (2.5 ng/mL) for the indicated time points. **(D)** Representative scratch wounds at the time point of 50 h in 50 μg/mL GD3-treated A549-VIM-RFP cells with or without TGF-β (2.5 ng/mL) are shown. Scale bar = 400 μm. **(E)** Oncomine database summary for *ST3GAL5* gene expression in various cancers. The comparison indicated the number of datasets with statistically significant *ST3GAL5* mRNA overexpression (red) and downregulated expression (blue) in cancers versus normal tissues. Colours reflect the best gene rank percentile for the analyses within the datasets. **(F)** Tissue microarray from lung cancer patients that were stained with anti-ST3GAL5. Representative images of lung cancer biopsies with adenocarcinoma and adjacent normal tissues are shown. Scale bar = 100 μm. **(G)** Scatter plot of ST3GAL5 expression in lung normal tissues and lung cancer tissues of different stages. Each point represents the H-score from a single tissue sample ranging from the total absence of ST3GAL5 (H-score: 0) to very strong ST3GAL5 staining (H-score: 300). H-scores are represented as mean ± SEM, adjacent normal tissue, n=21; cancer adjacent lung tissue (adjacent tissue), n=27; adenocarcinoma (stage IA), n=4; adenocarcinoma (stage IB), n=59; adenocarcinoma (stage IIB), n=28; adenocarcinoma (stage IIIA), n=6; ****, $P < 0.0001$, based on an unpaired Student's t-test. Data information: In (A, C), data are expressed as mean ± SEM, n=3; no statistically significant difference, based on an unpaired Student's t-test.

Appendix Figures

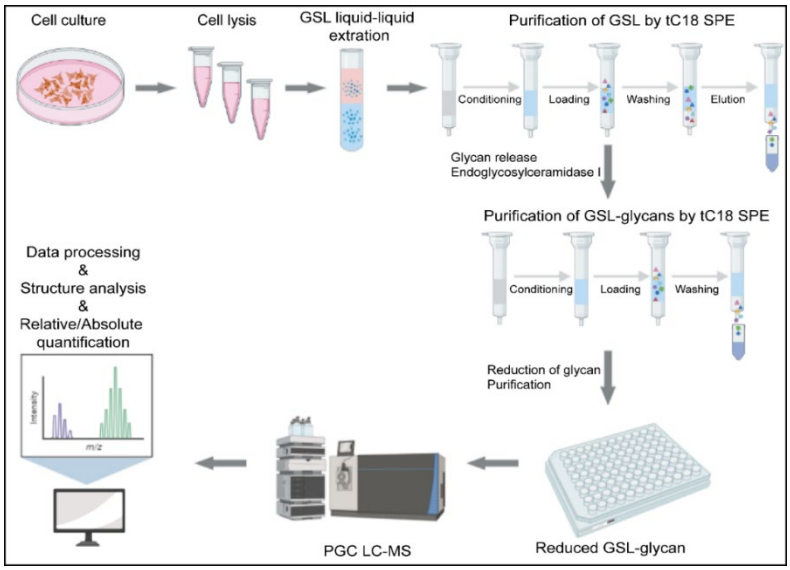

Appendix Figure S1. related to Figure 1. Workflow for preparation and analysis of glycosphingolipid (GSL)-glycans based on PGC nano-LC-ESI-MS/MS.

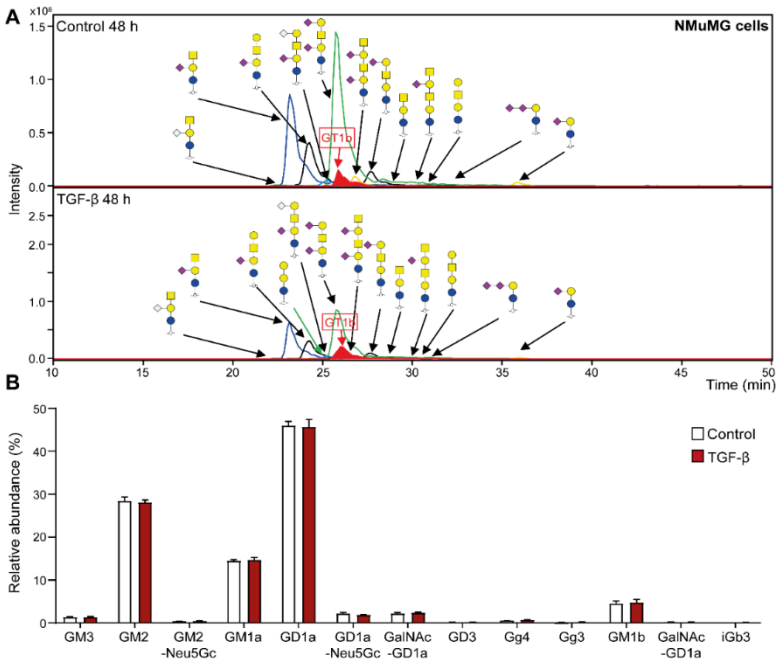

Appendix Figure S2. related to Figure 1. Abundance changes of GSL-glycans with or without TGF-β stimulation in NMuMG cells. (A) Extracted ion chromatograms

(EIC) of GSL-glycans released from NMuMG cells treated with TGF-β (2.5 ng/mL) for 48 h. **(B)** Relative abundance of individual GSL-glycans in NMuMG cells with vehicle control or TGF-β (2.5 ng/mL) for 48 h. Histograms give mean ± SD, n=3. unpaired Student's t test. Not statistically significant difference.

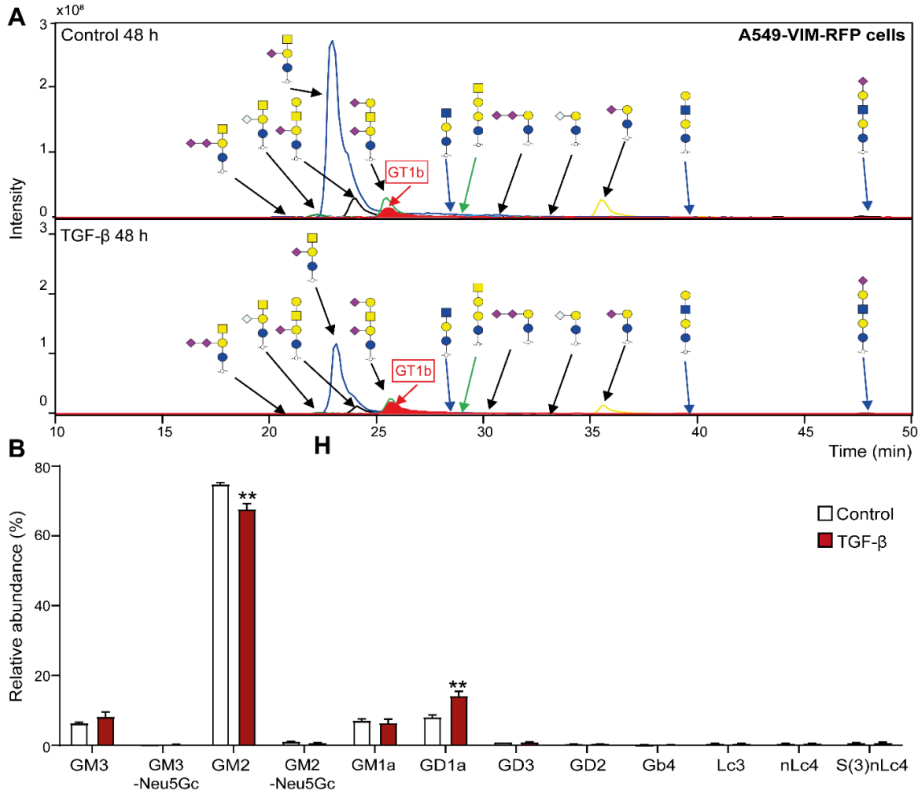

Appendix Figure S3. related to Figure 1. Abundance changes of GSL-glycans with or without TGF-β stimulation in A549 cells. (A) EIC of GSL-glycans released from A549-VIM-RFP cells treated with TGF-β (2.5 ng/mL) for 48 h. **(B)** Relative abundance of individual GSL-glycans in A549-VIM-RFP cells with vehicle control or TGF-β (2.5 ng/mL) for 48 h. Histograms give mean ± SD, n=3. **, $P < 0.01$, based on an unpaired Student's t-test.

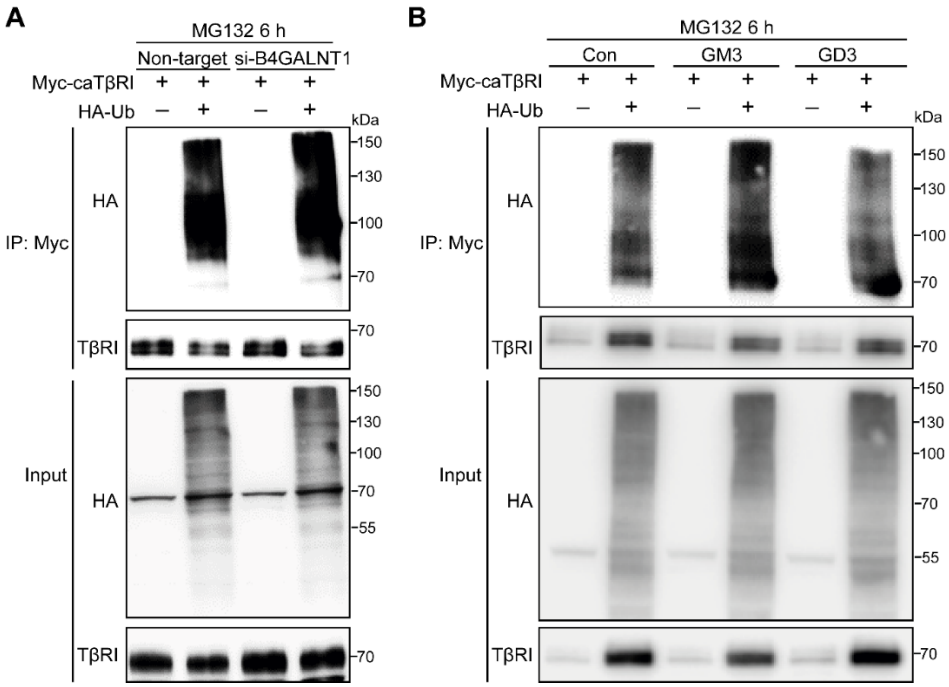

Appendix Figure S4, related to Figure 6. Knockdown of B4GALNT1 or exogenous GD3 addition has no effect on TβRI ubiquitination. (A) HEK293T cells transfected with Myc-tagged constitutively active TβRI (caTβRI), HA-Ubiquitin (HA-Ub) and non-targeting siRNA or B4GALNT1 siRNA, were collected for immunoprecipitation (IP) of anti-Myc antibody and immunoblot analysis. All the groups were treated with MG132 (5 μM) for 6 h. **(B)** Ubiquitination of TβRI was detected by IP of Myc-tagged caTβRI from HA-Ub transfected HEK293T cells with or without exogenous addition of GM3 (50 μg/ml) and GD3 (50 μg/ml) for 24 h. All the groups were treated with MG132 (5 μM) for 6 h.

References

1. Colak, S. and P. Ten Dijke, Targeting TGF-β Signaling in Cancer. Trends Cancer, 2017. 3(1): p. 56-71.
2. Massague, J., TGFβ in Cancer. Cell, 2008. 134(2): p. 215-30.
3. Massague, J., How cells read TGF-β signals. Nat Rev Mol Cell Biol, 2000. 1(3): p. 169-78.
4. Shi, Y. and J. Massague, Mechanisms of TGF-β signaling from cell membrane to the nucleus. Cell, 2003. 113(6): p. 685-700.
5. Heldin, C.H., K. Miyazono, and P. ten Dijke, TGF-β signalling from cell membrane to nucleus through SMAD proteins. Nature, 1997. 390(6659): p. 465-71.

6. ten Dijke, P. and C.S. Hill, New insights into TGF-β-Smad signalling. Trends Biochem Sci, 2004. 29(5): p. 265-73.
7. Tzavlaki, K. and A. Moustakas, TGF-β Signaling. Biomolecules, 2020. 10(3).
8. Levy, L. and C.S. Hill, Smad4 dependency defines two classes of transforming growth factor β (TGF-β) target genes and distinguishes TGF-β-induced epithelial-mesenchymal transition from its antiproliferative and migratory responses. Mol Cell Biol, 2005. 25(18): p. 8108-25.
9. Chen, Y.G., Endocytic regulation of TGF-β signaling. Cell Res, 2009. 19(1): p. 58-70.
10. Panopoulou, E., et al., Early endosomal regulation of Smad-dependent signaling in endothelial cells. J Biol Chem, 2002. 277(20): p. 18046-52.
11. Di Guglielmo, G.M., et al., Distinct endocytic pathways regulate TGF-β receptor signalling and turnover. Nat Cell Biol, 2003. 5(5): p. 410-21.
12. Mitchell, H., et al., Ligand-dependent and -independent transforming growth factor-β receptor recycling regulated by clathrin-mediated endocytosis and Rab11. Mol Biol Cell, 2004. 15(9): p. 4166-78.
13. Zhao, B. and Y.G. Chen, Regulation of TGF-β Signal Transduction. Scientifica (Cairo), 2014. 2014: p. 874065.
14. Hayashi, H., et al., The MAD-related protein Smad7 associates with the TGFβ receptor and functions as an antagonist of TGFβ signaling. Cell, 1997. 89(7): p. 1165-73.
15. Nakao, A., et al., Identification of Smad7, a TGFβ-inducible antagonist of TGF-β signalling. Nature, 1997. 389(6651): p. 631-5.
16. Katsuno, Y., S. Lamouille, and R. Derynck, TGF-β signaling and epithelial-mesenchymal transition in cancer progression. Curr Opin Oncol, 2013. 25(1): p. 76-84.
17. Lamouille, S., J. Xu, and R. Derynck, Molecular mechanisms of epithelial-mesenchymal transition. Nat Rev Mol Cell Biol, 2014. 15(3): p. 178-96.
18. Hu, W., et al., Ubiquitin specific peptidase 19 is a prognostic biomarker and affect the proliferation and migration of clear cell renal cell carcinoma. Oncol Rep, 2020. 43(6): p. 1964-1974.
19. Nakajima, Y., et al., Mechanisms involved in valvuloseptal endocardial cushion formation in early cardiogenesis: roles of transforming growth factor (TGF)-β and bone morphogenetic protein (BMP). Anat Rec, 2000. 258(2): p. 119-27.
20. Barriere, G., et al., Epithelial Mesenchymal Transition: a double-edged sword. Clin Transl Med, 2015. 4: p. 14.
21. Derynck, R. and R.A. Weinberg, EMT and Cancer: More Than Meets the Eye. Dev Cell, 2019. 49(3): p. 313-316.

22. Zeisberg, E.M., et al., Endothelial-to-mesenchymal transition contributes to cardiac fibrosis. Nat Med, 2007. 13(8): p. 952-61.
23. Derynck, R., B.P. Muthusamy, and K.Y. Saeteurn, Signaling pathway cooperation in TGF-β-induced epithelial-mesenchymal transition. Curr Opin Cell Biol, 2014. 31: p. 56-66.
24. Xu, Y., N. Uddin, and G.K. Wagner, Covalent Probes for Carbohydrate-Active Enzymes: From Glycosidases to Glycosyltransferases. Methods Enzymol, 2018. 598: p. 237-265.
25. Reily, C., et al., Glycosylation in health and disease. Nat Rev Nephrol, 2019. 15(6): p. 346-366.
26. Schnaar, R.L. and T. Kinoshita, Glycosphingolipids, in Essentials of Glycobiology, rd, et al., Editors. 2015: Cold Spring Harbor (NY). p. 125-135.
27. Regina Todeschini, A. and S.I. Hakomori, Functional role of glycosphingolipids and gangliosides in control of cell adhesion, motility, and growth, through glycosynaptic microdomains. Biochim Biophys Acta, 2008. 1780(3): p. 421-33.
28. Coskun, U., et al., Regulation of human EGF receptor by lipids. Proc Natl Acad Sci U S A, 2011. 108(22): p. 9044-8.
29. Kabayama, K., et al., Dissociation of the insulin receptor and caveolin-1 complex by ganglioside GM3 in the state of insulin resistance. Proc Natl Acad Sci U S A, 2007. 104(34): p. 13678-83.
30. Pontier, S.M. and F. Schweisguth, Glycosphingolipids in signaling and development: from liposomes to model organisms. Dev Dyn, 2012. 241(1): p. 92-106.
31. Kawashima, N., et al., Tyrosine kinase activity of epidermal growth factor receptor is regulated by GM3 binding through carbohydrate to carbohydrate interactions. J Biol Chem, 2009. 284(10): p. 6147-55.
32. Li, X., et al., Role of Glycans in Cancer Cells Undergoing Epithelial-Mesenchymal Transition. Front Oncol, 2016. 6: p. 33.
33. Zhang, J., et al., Role of glycosylation in TGF-β signaling and epithelial-to-mesenchymal transition in cancer. Protein Cell, 2021. 12(2): p. 89-106.
34. Guan, F., K. Handa, and S.I. Hakomori, Specific glycosphingolipids mediate epithelial-to-mesenchymal transition of human and mouse epithelial cell lines. Proc Natl Acad Sci U S A, 2009. 106(18): p. 7461-6.
35. Zhang, J., et al., Studying TGF-β Signaling and TGF-β-induced Epithelial-to-mesenchymal Transition in Breast Cancer and Normal Cells. J Vis Exp, 2020(164).
36. Wang, W., et al., Live-cell imaging and analysis reveal cell phenotypic transition dynamics inherently missing in snapshot data. Sci Adv, 2020. 6(36).

37. Anugraham, M., et al., A platform for the structural characterization of glycans enzymatically released from glycosphingolipids extracted from tissue and cells. Rapid Commun Mass Spectrom, 2015. 29(7): p. 545-61.
38. Zhang, T., et al., Differential O- and Glycosphingolipid Glycosylation in Human Pancreatic Adenocarcinoma Cells With Opposite Morphology and Metastatic Behavior. Front Oncol, 2020. 10: p. 732.
39. Rojas-Macias, M.A., et al., Towards a standardized bioinformatics infrastructure for N- and O-glycomics. Nat Commun, 2019. 10(1): p. 3275.
40. Allende, M.L. and R.L. Proia, Simplifying complexity: genetically resculpting glycosphingolipid synthesis pathways in mice to reveal function. Glycoconj J, 2014. 31(9): p. 613-22.
41. Stirnemann, J., et al., A Review of Gaucher Disease Pathophysiology, Clinical Presentation and Treatments. Int J Mol Sci, 2017. 18(2).
42. Simons, K. and E. Ikonen, Functional rafts in cell membranes. Nature, 1997. 387(6633): p. 569-72.
43. Mukherjee, S. and F.R. Maxfield, Membrane domains. Annu Rev Cell Dev Biol, 2004. 20: p. 839-66.
44. von Zastrow, M. and A. Sorkin, Signaling on the endocytic pathway. Curr Opin Cell Biol, 2007. 19(4): p. 436-45.
45. Anderson, R.G. and K. Jacobson, A role for lipid shells in targeting proteins to caveolae, rafts, and other lipid domains. Science, 2002. 296(5574): p. 1821-5.
46. Gyorffy, B., et al., Online survival analysis software to assess the prognostic value of biomarkers using transcriptomic data in non-small-cell lung cancer. PLoS One, 2013. 8(12): p. e82241.
47. Neapolitan, R., C.M. Horvath, and X. Jiang, Pan-cancer analysis of TCGA data reveals notable signaling pathways. BMC Cancer, 2015. 15: p. 516.
48. Saha, S.K., et al., PROM1 and PROM2 expression differentially modulates clinical prognosis of cancer: a multiomics analysis. Cancer Gene Ther, 2020. 27(3-4): p. 147-167.
49. Cabarcas-Petroski, S., P.I. Meneses, and L. Schramm, A meta-analysis of BRF2 as a prognostic biomarker in invasive breast carcinoma. BMC Cancer, 2020. 20(1): p. 1093.
50. Granville, C.A. and P.A. Dennis, An overview of lung cancer genomics and proteomics. Am J Respir Cell Mol Biol, 2005. 32(3): p. 169-76.
51. Bhattacharjee, A., et al., Classification of human lung carcinomas by mRNA expression profiling reveals distinct adenocarcinoma subclasses. Proc Natl Acad Sci U S A, 2001. 98(24): p. 13790-5.
52. Kim, S.J., et al., Ganglioside GM3 participates in the TGF-β1-induced epithelial-mesenchymal transition of human lens epithelial cells. Biochem J, 2013. 449(1): p. 241-51.

53. Sarkar, T.R., et al., GD3 synthase regulates epithelial-mesenchymal transition and metastasis in breast cancer. Oncogene, 2015. 34(23): p. 2958-67.
54. Li, T., et al., Chemoenzymatic synthesis and biological evaluation of ganglioside GM3 and lyso-GM3 as potential agents for cancer therapy. Carbohydr Res, 2021. 509: p. 108431.
55. Prinetti, A., et al., A glycosphingolipid/caveolin-1 signaling complex inhibits motility of human ovarian carcinoma cells. J Biol Chem, 2011. 286(47): p. 40900-10.
56. Satoh, M., et al., Enhanced GM3 expression, associated with decreased invasiveness, is induced by brefeldin A in bladder cancer cells. Int J Oncol, 2001. 19(4): p. 723-31.
57. Ouyang, S., et al., Downregulation of ST3GAL5 is associated with muscle invasion, high grade and a poor prognosis in patients with bladder cancer. Oncol Lett, 2020. 20(1): p. 828-840.
58. Kan, J.Y., et al., Comprehensive Transcriptomic Analysis Identifies ST8SIA1 as a Survival-Related Sialyltransferase Gene in Breast Cancer. Genes (Basel), 2020. 11(12).
59. Lloyd, K.O. and L.J. Old, Human monoclonal antibodies to glycolipids and other carbohydrate antigens: dissection of the humoral immune response in cancer patients. Cancer Res, 1989. 49(13): p. 3445-51.
60. Hakomori, S., Tumor malignancy defined by aberrant glycosylation and sphingo(glyco)lipid metabolism. Cancer Res, 1996. 56(23): p. 5309-18.
61. Jensen, P.H., et al., Structural analysis of N- and O-glycans released from glycoproteins. Nat Protoc, 2012. 7(7): p. 1299-310.
62. Karlsson, N.G., et al., Negative ion graphitised carbon nano-liquid chromatography/mass spectrometry increases sensitivity for glycoprotein oligosaccharide analysis. Rapid Commun Mass Spectrom, 2004. 18(19): p. 2282-92.
63. Karlsson, N.G., B.L. Schulz, and N.H. Packer, Structural determination of neutral O-linked oligosaccharide alditols by negative ion LC-electrospray-MSn. J Am Soc Mass Spectrom, 2004. 15(5): p. 659-72.
64. Ceroni, A., et al., GlycoWorkbench: a tool for the computer-assisted annotation of mass spectra of glycans. J Proteome Res, 2008. 7(4): p. 1650-9.
65. Cooper, C.A., E. Gasteiger, and N.H. Packer, GlycoMod--a software tool for determining glycosylation compositions from mass spectrometric data. Proteomics, 2001. 1(2): p. 340-9.
66. Jongsma, M.L.M., et al., The SPPL3-Defined Glycosphingolipid Repertoire Orchestrates HLA Class I-Mediated Immune Responses. Immunity, 2021. 54(1): p. 132-150 e9.

67. Sanjana, N.E., O. Shalem, and F. Zhang, Improved vectors and genome-wide libraries for CRISPR screening. Nat Methods, 2014. 11(8): p. 783-784.
68. Shalem, O., et al., Genome-scale CRISPR-Cas9 knockout screening in human cells. Science, 2014. 343(6166): p. 84-87.
69. Hunter, F.W., et al., Functional CRISPR and shRNA Screens Identify Involvement of Mitochondrial Electron Transport in the Activation of Evofosfamide. Mol Pharmacol, 2019. 95(6): p. 638-651.
70. Gajate, C. and F. Mollinedo, Isolation of Lipid Rafts Through Discontinuous Sucrose Gradient Centrifugation and Fas/CD95 Death Receptor Localization in Raft Fractions. Methods Mol Biol, 2017. 1557: p. 125-138.
71. Ren, J., et al., Invasive Behavior of Human Breast Cancer Cells in Embryonic Zebrafish. J Vis Exp, 2017(122).
72. Rhodes, D.R., et al., Oncomine 3.0: genes, pathways, and networks in a collection of 18,000 cancer gene expression profiles. Neoplasia, 2007. 9(2): p. 166-80.
73. Rhodes, D.R., et al., ONCOMINE: a cancer microarray database and integrated data-mining platform. Neoplasia, 2004. 6(1): p. 1-6.
74. Subramanian, A., et al., Gene set enrichment analysis: a knowledge-based approach for interpreting genome-wide expression profiles. Proc Natl Acad Sci U S A, 2005. 102(43): p. 15545-50.
75. Mootha, V.K., et al., PGC-1alpha-responsive genes involved in oxidative phosphorylation are coordinately downregulated in human diabetes. Nat Genet, 2003. 34(3): p. 267-73.
76. Coulouarn, C., V.M. Factor, and S.S. Thorgeirsson, Transforming growth factor-β gene expression signature in mouse hepatocytes predicts clinical outcome in human cancer. Hepatology, 2008. 47(6): p. 2059-67.
77. Padua, D., et al., TGFβ primes breast tumors for lung metastasis seeding through angiopoietin-like 4. Cell, 2008. 133(1): p. 66-77.
78. Gotzmann, J., et al., A crucial function of PDGF in TGF-β-mediated cancer progression of hepatocytes. Oncogene, 2006. 25(22): p. 3170-85.
79. Sarrio, D., et al., Epithelial-mesenchymal transition in breast cancer relates to the basal-like phenotype. Cancer Res, 2008. 68(4): p. 989-97.
80. Zhou, F., et al., Nuclear receptor NR4A1 promotes breast cancer invasion and metastasis by activating TGF-β signalling. Nat Commun, 2014. 5: p. 3388.